Laser/Lidar Analysis and Testing

Contract No. NAS8-38609

Delivery Order No. 38

Contract Period 5/13/92 - 5/12/93

Report Date 2/23/94

Gary D. Spiers
Center for Applied Optics
University of Alabama in Huntsville
Huntsville
AL 35899
(205) 895 6030 ext. 448

(NASA-CR-193954) LASER/LIDAR ANALYSIS AND TESTING Final Report, 13 May 1992 - 12 May 1993 (Alabama Univ.) 70 p

N94-34136

Unclas

G3/36 0008463

Introduction 2

1.0 Frequency Spectrum of a Pulsed CO_2 Laser 3
- 1.1 Introduction 3
- 1.2 Pulse Shape Model 3
- 1.3 Frequency Chirp Model 5
  - 1.3.1 Laser Induced Medium Perturbation 5
  - 1.3.2 Plasma Frequency Chirp 7
- 1.4 Pulse Frequency Spectrum 9
- 1.5 Results 10
- 1.6 Comparison with Experimental Results 13
  - 1.6.1 Comparison with the NOAA Laser. 14
  - 1.6.2 Comparison with the STI Optronics LAWS Breadboard. 17
  - 1.6.3 Comparison with the Textron Defense Systems LAWS Breadboard 19
- 1.7 Summary 19
- 1.8 References 20

2.0 LAWS Laser Breadboard Results 21
- 2.1 Introduction 21
  - 2.1.1 Measurements Made 21
- 2.2 Textron Defense Systems 23
  - 2.2.1 General Comments 23
  - 2.2.2 Performance 24
    - 2.2.2.1 Output Pulse Energy, Intensity Profile and Efficiency 24
    - 2.2.2.2 Single Mode Performance 25
    - 2.2.2.3 Frequency Chirp / Frequency Spectrum 25
    - 2.2.2.4 Operation at High Pulse Rates 26
- 2.3 STI Optronics 27
  - 2.3.1 General Comments 27
  - 2.3.2 Performance 28
    - 2.3.2.1 Output Pulse Energy, Intensity Profile and Efficiency. 29
    - 2.3.2.2 Single Mode Performance 30
    - 2.3.2.3 Frequency Chirp / Frequency Spectrum 30
    - 2.3.2.4 Operation at High Pulse Rates 31
- 2.4 Summary and Conclusions 32

3.0 LAWS Power Budget on a Spot MK2 Platform 33
- 3.1 Introduction 33
- 3.2 Power System 33
  - 3.2.1 Spacecraft Power 33
  - 3.2.2 Instrument Power 33
- 3.3 Orbit parameters 34
- 3.4 Laser Power Requirements 35
  - 3.4.1 Effect of scan pattern. 35
  - 3.4.2 Latitude dependent effects. 35
- 3.5 38
- 3.6 Results 39
- 3.7 Conclusions 42
- 3.8 References 42

A1 Appendix 1 - TDS Breadboard Results A1.1

A2 Appendix 2 - STI Optronics Breadboard Results A2.1

A3 Appendix 3 - LAWS Instrument Power Requirements A3.1

Introduction

This report details work carried out on NASA contract NAS8-38609 delivery order no. 38. Section 1 outlines work on the development of a simple model for the frequency chirp mechanisms and frequency spectra of pulsed CO_2 lasers.The validity of the model is verified by comparison with experimental results from the LAWS laser breadboards and from the NOAA laser transmitter. This work resulted in a paper at the 3rd International DRA/NASA Conference on Long-Life CO_2 Laser Technology [0.1].

Section 2 and Appendices 1 and 2 report on a visit to the LAWS laser contractors to measure the performance of the laser breadboards.

Section 2 and Appendices 1 and 2 contain information gathered during visits to the LAWS laser breadboard contractors. Some of this information may be regarded as competitively sensitive by the contractors.

Section 3 and Appendix 3 report on a model developed to assess the power requirements of a 5 J LAWS instrument on a Spot MKII platform in a polar orbit. The performance was assessed for three different latitude dependent sampling strategies.

[0.1] G.D. Spiers, "Numerical Modeling for the NASA Laser Atmospheric Wind Sounder", Proc. 3rd. International DRA/NASA Conference on Long-Life CO_2 Laser Technology, 10th - 12th November, 1992, Malvern, UK.

1.0 Frequency Spectrum of a Pulsed CO_2 Laser

1.1 Introduction

This chapter details development of a model of the output pulse frequency spectrum of a pulsed transversely excited (TE) CO_2 laser. In order to limit the computation time required, the model was designed around a generic laser pulse shape model (Section 1.2, page 2). The use of such a procedure allows many possible laser configurations to be examined. The output pulse shape is combined with the calculated frequency chirp to produce the electric field of the output pulse which is then computationally mixed with a local oscillator field to produce the heterodyne beat signal that would fall on a detector. The power spectral density of this heterodyne signal is then calculated.

Intrapulse frequency variations, or chirp, in the output of TEA CO_2 lasers first reported in 1973 [1.1][1.2], since when several additional studies have appeared [1.3][1.4][1.5][1.6][1.7]. The frequency chirp arises due to changes in the effective cavity length during the pulse formation.

Some of these publications [1.1][1.2] attributed this chirping phenomena as being partly due to refractive index changes in the laser medium caused by anomalous dispersion effects arising from small offsets of the laser frequency from line centre. It has since been shown [1.3][1.5][1.8] that this process can account for only a fraction of the measured chirp rate. Gas density perturbations due to acoustic shock waves originating at the electrodes during the discharge [1.2][1.9] have also been suggested as possible causes of the frequency chirp. This mechanism is relatively slow [1.8] and only becomes effective in the optical pulse tail after several microseconds have elapsed.

More recent analysis of chirp inducing phenomena [1.8][1.10][1.11] has allowed theoretical considerations to fit the observed frequency chirping. Two main processes were identified, the effect of the time varying gas density due to thermal expansion of the gas and the effect of the time varying electron density in the laser discharge plasma.

1.2 Pulse Shape Model

The optical output pulse from a transversely excited CO_2 laser can be divided into three components, an initial gain switched spike, an approximately flat plateau region and a decaying pulse tail. In some devices the flat plateau region may be missing, depending on the laser parameters such as discharge pulse duration and gas composition and pressure. For the purposes of this analysis, the pulse gain switch profile can be represented by a gaussian. The time dependent intensity of the optical pulse can then be represented as:-

$$I(t) = \begin{cases} e^{-8t^2/\tau^2_{rise}} & 0 < t < (\tau_{rise} + \tau_{fall}) \\ I_r & \text{where } (\tau_{rise} + \tau_{fall}) < t < \tau_{flat} \\ I_r e^{-2t/\tau_{relax}} & \tau_{flat} < t \end{cases} \quad (1.1)$$

with:-

$$\tau_{fall} = \sqrt{-\frac{\tau_{rise}^2}{8}\ln(I_r)} \tag{1.2}$$

$$\tau_{flat} = FWHM - \tau_{tail} - \tau_{rise} - \tau_{fall} \tag{1.3}$$

$$\tau_{tail} = -\frac{\tau_{relax}}{2}\ln(0.5) \tag{1.4}$$

where τ_{rise} is the gain switched spike rise time, τ_{fall} is the time for the gain switched spike intensity to fall to the plateau value, τ_{relax} is the relaxation rate of the electric field in the tail of the pulse, FWHM is the full width half maximum of the pulse relative to the flat portion of the pulse and I_r is the ratio of the intensity in the flat portion of the pulse to the intensity at the peak of the gain switched spike. Thus the pulse can be fully defined by the four parameters τ_{rise},τ_{relax}, FWHM and I_r enabling different pulse intensity profiles to be easily generated. Once the pulse profile has been obtained, the pulse intensity can be normalised to provide the required total pulse energy.Figure (1.1) shows a 20 J pulse where τ_{rise},τ_{relax}, FWHM and I_r have the values 100 ns, 3 µs, 3 µs and 0.57 respectively. The figure also shows the pulse energy evolution as a function of time. The pulse generated in this way is then used to calculate the laser induced medium perturbation (LIMP) frequency chirp.

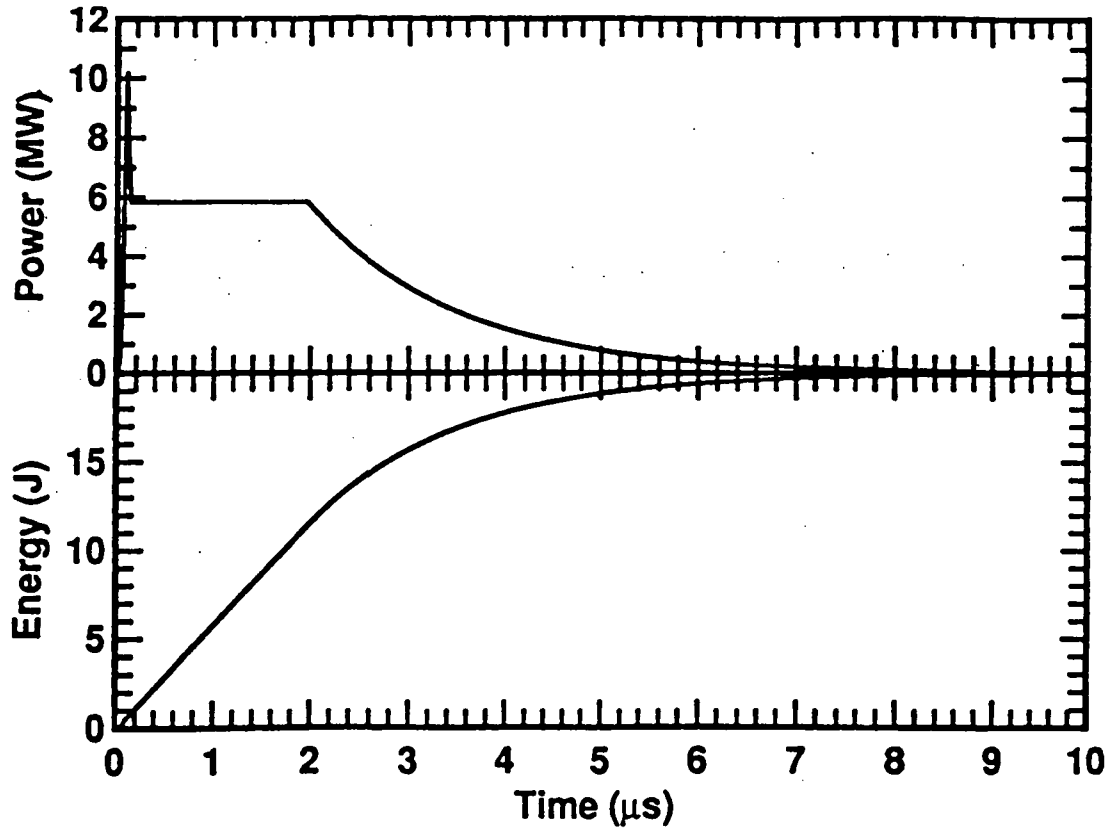

Figure (1.1) A typical pulse generated using the pulse shape generator discussed in the text. The values used for τ_{rise},τ_{relax}, FWHM and I_r were 100 ns, 3 µs, 3 µs and 0.57 respectively. Also shown is the pulse energy evolution as a function of time.

1.3 Frequency Chirp Model

1.3.1 Laser Induced Medium Perturbation

Laser induced medium perturbation (LIMP) arises as a consequence of the extraction of the optical radiation from the laser medium. Lasing occurs in the CO_2 laser between two vibrational states of the CO_2 molecule with the rotational sub-structure of these vibrational states providing the line structure of the laser transition. Each photon produced in the laser leaves behind a CO2 molecule in the lower laser level, which is the 100 or 020 vibrational level depending on the laser transition. CO_2 molecules in these vibrational states loose this vibrational energy by collision with a CO_2 molecule in its ground state to produce two molecules in the 010 vibrational level, each with half the original vibrational energy. The CO_2 molecules in the 010 level decay to the ground state by collision with He molecules which results in the transfer of the CO_2 vibrational energy into translational (thermal) energy of the He molecule. As a consequence of the mode pattern within the resonator, this heat deposition is non uniform and leads to thermal gradients within the gas which drive a fluid dynamic expansion. This results in a drop in gas density and refractive index near regions of high intensity. This relaxation process is sufficiently fast such that the refractive index will sweep with the pulse intensity profile so that the resonant frequency of the cavity chirps during the laser pulse formation.

Willetts and Harris [1.8] have shown that the time dependent density perturbation within the gain volume is given, to the first order, by:

$$\frac{\partial \rho}{\partial t} = \frac{R}{C_v} \nabla^2 \left(\frac{E}{V}\right) t \tag{1.5}$$

where R is the molar gas constant, C_v is the specific heat capacity at constant volume, ρ is the gas density, V is the mode volume and E is the optical pulse energy. This is valid provided that the condition:

$$v_s t \ll \sigma \tag{1.6}$$

where v_s is the sound velocity in the gas and σ is the laser spot radius in the gain region, is satisfied.

They showed [1.8][1.10] that the Laplacian operator ∇^2 can be replaced by the approximation:

$$\nabla^2 \left(\frac{E}{V}\right) = \frac{-4E}{\pi \sigma^4 l} \left(\frac{\nu_0}{\nu}\right) \tag{1.7}$$

where l is the gain length, ν_0 and ν are the equivalent frequency of the CO_2 lower laser level and the frequency of the output photons respectively.

The refractive index of the gas forming the discharge volume is related to its density by:

$$\frac{\partial n}{\partial t} = K\frac{\partial \rho}{\partial t} \tag{1.8}$$

where K is the Gladstone-Dale constant $(dn/d\rho)$. The frequency chirp $d\nu$ caused by a refractive index change, d is given by:

$$\frac{d\nu}{\nu} = \frac{-l}{L}\frac{dn}{n} \tag{1.9}$$

where l/L is the proportion of the cavity length, L occupied by the gain medium. Combining and then integrating equations (1.9), (1.8), (1.7) and (1.5) gives a frequency chirp $\Delta\upsilon(t)$ of:

$$\Delta\nu(t) = \frac{2KR\nu_0 E}{\pi LC_v\sigma^4 n}t^2 \tag{1.10}$$

This expression, which was derived by Willetts and Harris is valid for short pulses in which most of the energy is deposited in the gain switched spike. For long pulses they modified this to:

$$\Delta\nu(t) = \frac{2KR\nu_0 Et^3}{3\pi LC_v\sigma^4\tau} \tag{1.11}$$

where τ is the optical pulse length and the refractive index, n has been set to unity. This expression assumes a linear deposition of energy into the thermal heating i.e. a square output pulse. In practise this is not the case and so for this work equation (1.11) was modified to account for the time dependence of the output pulse energy. This gives:

$$\Delta\nu(t) = \frac{2KR\nu_0 E(t)t^2}{3\pi LC_v\sigma^4} \tag{1.12}$$

for the time dependent frequency chirp due to the laser induced medium perturbation.

It can be seen that the LIMP frequency chirp is very sensitive to the value of the mode spot radius, σ. The above derivation assumed a stable resonator with a TEM00 Gaussian mode. The lasers of interest to the LAWS project use unstable resonators and for a confocal unstable resonator with a super-Gaussian reflectance profile output coupler the mode spot radius can be approximated using[1.12]:-

$$\sigma = \sigma_m(M^n - 1)^{1/n} \tag{1.13}$$

where σ_m is the $1/e^2$ radius of the super-Gaussian output coupler, M is the cavity magnification and n is the super-Gaussian order. Conventional unstable resonators can be approximated by setting n to a large number such as 200.

1.3.2 Plasma Frequency Chirp

The refractive index variation associated with the time-dependent electron density in the decaying discharge plasma occurs mainly during the build-up time of the optical pulse. This electron density decay coincides with the trailing edge of the electrical current pulse and causes a down chirp in the output pulse frequency as the electron density becomes small. For a device which has a constant electron density during the pulse formation process, for example an electron beam sustained device, there will be no plasma induced frequency chirp [1.11].

The refractive index of an electron-plasma for an optical signal with angular frequency, ω is given by:

$$n^2 = 1 - \frac{\omega_p^2}{\omega^2} \tag{1.14}$$

where ω_p is the plasma frequency given by:

$$\omega_p^2 = \frac{N_e q_e^2}{\varepsilon_0 m_e} \tag{1.15}$$

where q_e and m_e are the charge and mass, respectively, of an electron, ε_0 is the permittivity of free space and N_e is the volumetric number density of the electrons in the plasma. Rearranging (1.14) gives:

$$n = \left[1 + \left(\frac{-\omega_p^2}{\omega^2}\right)\right]^{0.5} \tag{1.16}$$

which can be expanded using:

$$(1+x)^n = 1 + nx + \frac{n(n-1)}{2!}x^2 + \frac{n(n-1)(n-2)}{3!}x^3 + \ldots + \binom{n}{r}x^r + \ldots \tag{1.17}$$

provided $|x| < 1$. Typically the electron number density has a maximum of $\sim 10^{14}$ cm^{-3} giving a maximum value of $\sim 5.6 \times 10^{11}$ Hz for ω_p. Now $\omega - 1.8 \times 10^{14}$ Hz and as $\omega_p \ll \omega$ the above expansion is valid. Using only the first order terms gives:

$$n = 1 - \frac{\omega_p^2}{2\omega^2} \tag{1.18}$$

Combining this with equation (1.15) gives:

$$n = 1 - \frac{q_e^2 \lambda^2 N_e}{8\pi^2 \varepsilon_0 m_e c^2} \tag{1.19}$$

Combining this with equation (1.9) gives a plasma induced frequency chirp of:

$$\Delta\nu(t) = \frac{l q_e \lambda \Delta N_e(t)}{8\pi^2 \varepsilon_0 m_e c L n_0} \tag{1.20}$$

where n_0 is the initial refractive index, and the time dependence of the electron density has been included. In order to determine the time dependent electron density, $\Delta N_e(t)$, two approaches were considered.

The first approach assumed a maximum initial value for the electron number density at the start of the optical pulse and that the number density decays with a simple exponential:

$$N_e(t) = N_e^{pk} e^{\left(-\frac{t}{\tau_d}\right)} \tag{1.21}$$

where N_e^{pk} is the maximum electron number density and τ_d is the relaxation rate of the electron number density.

The second method calculates Ne(t) from:

$$N_e(t) = \frac{J(t)}{q_e v_d(t)} \tag{1.22}$$

where J(t) is the time varying discharge current density and $v_d(t)$ is the time varying electron drift velocity. Strictly speaking, equation (1.22) is only valid for steady state discharge conditions, however a more accurate calculation of $N_e(t)$ becomes numerically intensive and for the discharge conditions being considered here would only provide a small difference in the value of $N_e(t)$. Figure (1.2), taken from Elliot et al. [1.13] shows that the electron drift velocity has an approximately linear dependence on the reduced electric field, E/N and so can be modeled as:

$$v_d(t) = a + bE/N(t) \tag{1.23}$$

where a and b are determined by fitting a straight line to the drift velocity dependence on E/N. Obviously a Boltzmann code solution is required for each gas mixture considered. The value of E/N(t) is readily obtained from the discharge voltage, V(t) which can be approximated using simple pulse shapes. This series of approximations enables $N_e(t)$ to be determined. In practise it is easier and simpler to use the first method of estimating the electron density.

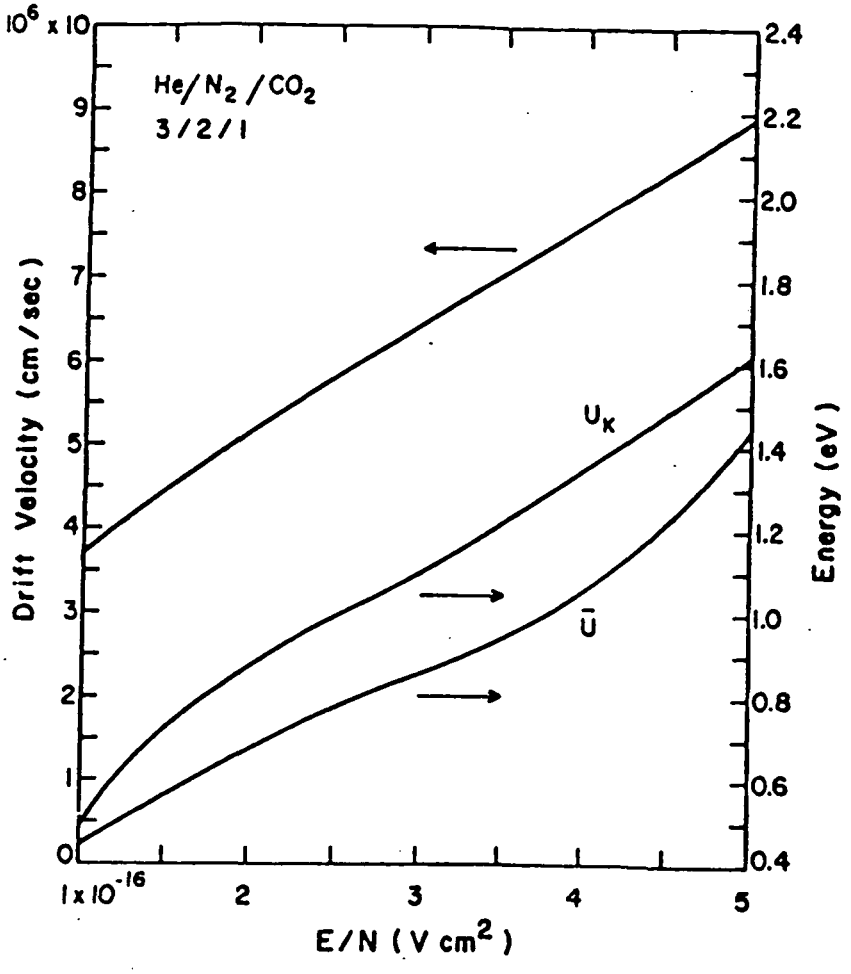

Figure (1.2) The electron drift velocity dependence on the reduced electric field (From Reference [1.13]).

1.4 Pulse Frequency Spectrum

Once the pulse intensity profile and frequency chirp have been calculated they are combined numerically with each other and with a local oscillator signal to provide a complex heterodyne beat frequency signal. This gives:

$$E1(t) = \sqrt{I(t)}\, e^{-2\pi i\left(\int \Delta\nu(t)\,dt + \nu_{lo}t\right)} \tag{1.24}$$

where E1(t) is the complex electric field that would be generated on a detector and ν_{lo} is the frequency offset of the local oscillator from the output pulse frequency. The local oscillator intensity has been normalised to 1 W for these calculations. The power spectrum of the laser pulse is then obtained by taking the modulus of the Fourier transform of E1(t) and squaring it:

1.5 Results

The frequency chirps for four different possibilities are shown in Figure (1.3). All the pulses used the intensity profile shown in Figure (1.1) and contain the same LIMP frequency chirp, calculated with values of 0.021 m, 5.1 m, 38.9 THz, 17.92 J/(Kmol) and 2.112×10^{-4} m^3/Kg for σ, L, ν_0, C_v and K respectively. These values are typical of those likely to occur in a 20 J laser suitable for the LAWS mission.

The first frequency chirp profile (Figure (1.3)a) represents the case where the discharge pulse is completed and the electron density has decayed before the start of the laser pulse, i.e. only LIMP frequency chirp is present in the pulse.

The remaining three pulses all contain varying amounts of plasma chirp and used values of 9.11 μm and 1.4 m for λ and l respectively. All assume that the peak electron density occurs at the start of the laser pulse and decays during the initial portion of the optical pulse to provide the maximum possible plasma induced frequency chirp. The devices under consideration for LAWS operate at sub-atmospheric pressure, use input energy densities which are low (<200 J/(L-Atm.)) and have pulse forming networks which limit the peak discharge current. These conditions lead to peak electron densities of ~10^{12} cm^{-3}. Preliminary measurements of the laser parameters (Section 2.0) indicate that for the purposes of this model a value of τ_d of ~(1-2) μs seems reasonable. The peak electron density was taken to be 1×10^{12} cm^{-3} for Figure (1.3)b and Figure (1.3)d, whilst Figure (1.3)c used a value of 5×10^{12} cm^{-3}. Figure (1.3)b and Figure (1.3)c used a value of 2 μs for τ_d whilst Figure (1.3)d used a value of 1 μs.

The frequency chirps in Figure (1.3) were combined numerically with the pulse intensity profile (Figure (1.2)) and with a local oscillator offset by 30 MHz from the laser and the power spectral density for each case was calculated. These are shown in Figure (1.4)b-e which also includes the power spectral density for a chirp free laser with the same intensity profile (Figure (1.4)a.

It can be seen that the frequency chirp shifts the spectral peak to frequencies greater than the local oscillator offset frequency, as might be expected, and spreads energy from the main lobe of the power spectrum into the higher frequencies. In order to be able to make an accurate velocity measurement, as much of the pulse energy as possible should be centered in a narrow bandwidth about the peak of the power spectrum. The energy contained in a 300 kHz bandwidth about the largest peak in each of the power spectra is given in Table (1.1). It can be seen that in all cases the energy in the 300 kHz bandwidth is significantly less than for the chirp free pulse. The LIMP chirp is seen to provide a high frequency content pulse tail as described previously. Elimination of this higher frequency content would require the reduction of the LIMP chirp or the elimination of the pulse tail.

The plasma chirp represents a more serious problem, due to the linear dependence of the plasma chirp on the electron density. The difference between Figure (1.4)c and Figure (1.4)d indicates the need to keep the electron density change as low as possible during the laser pulse. Figure (1.4)d clearly shows the spreading of the laser pulse energy into the higher frequencies as a consequence of the considerable frequency chirp during the main portion of the laser pulse.

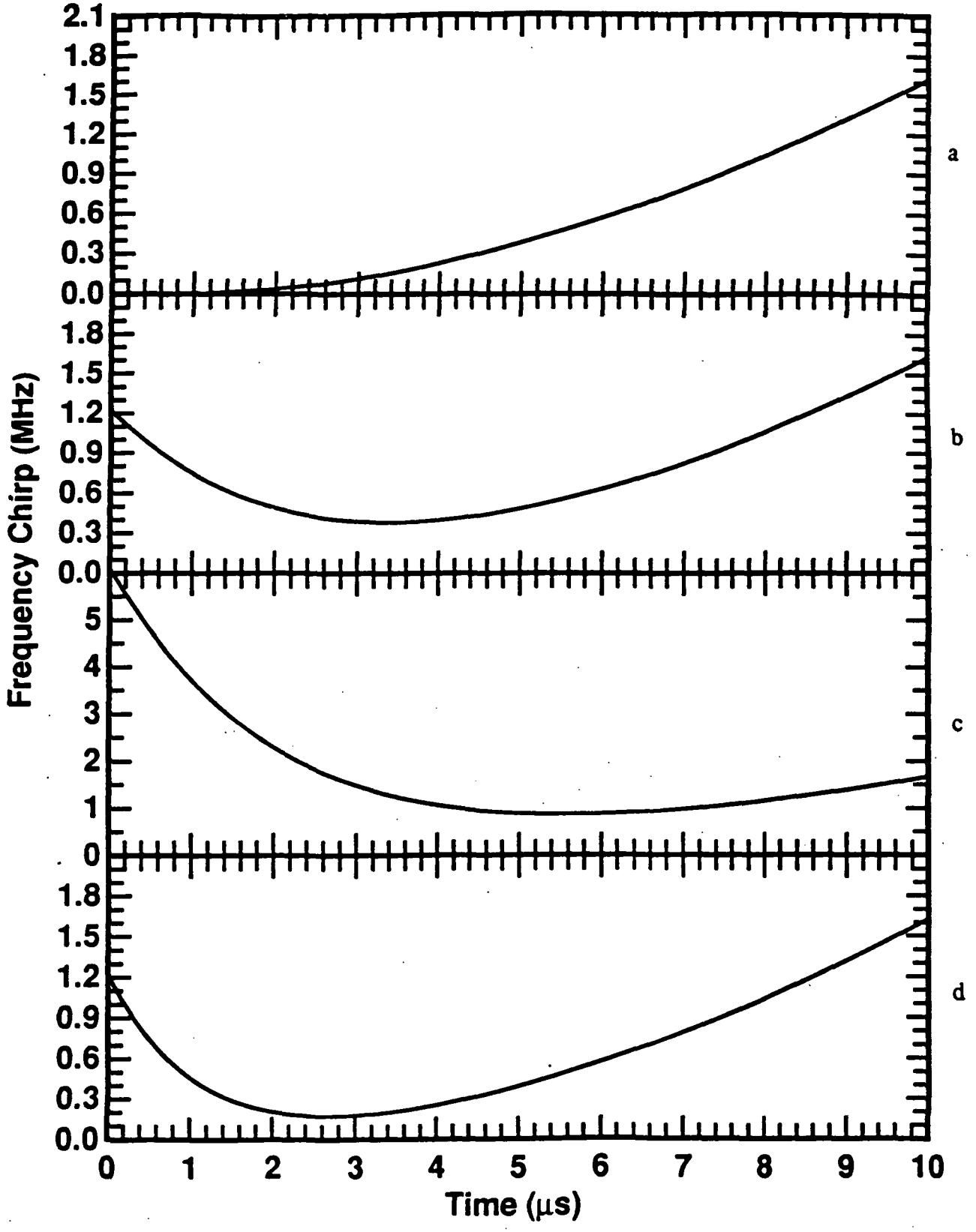

Figure (1.3) Time dependent laser pulse frequency chirp waveforms generated by the model *(see text for details)*.

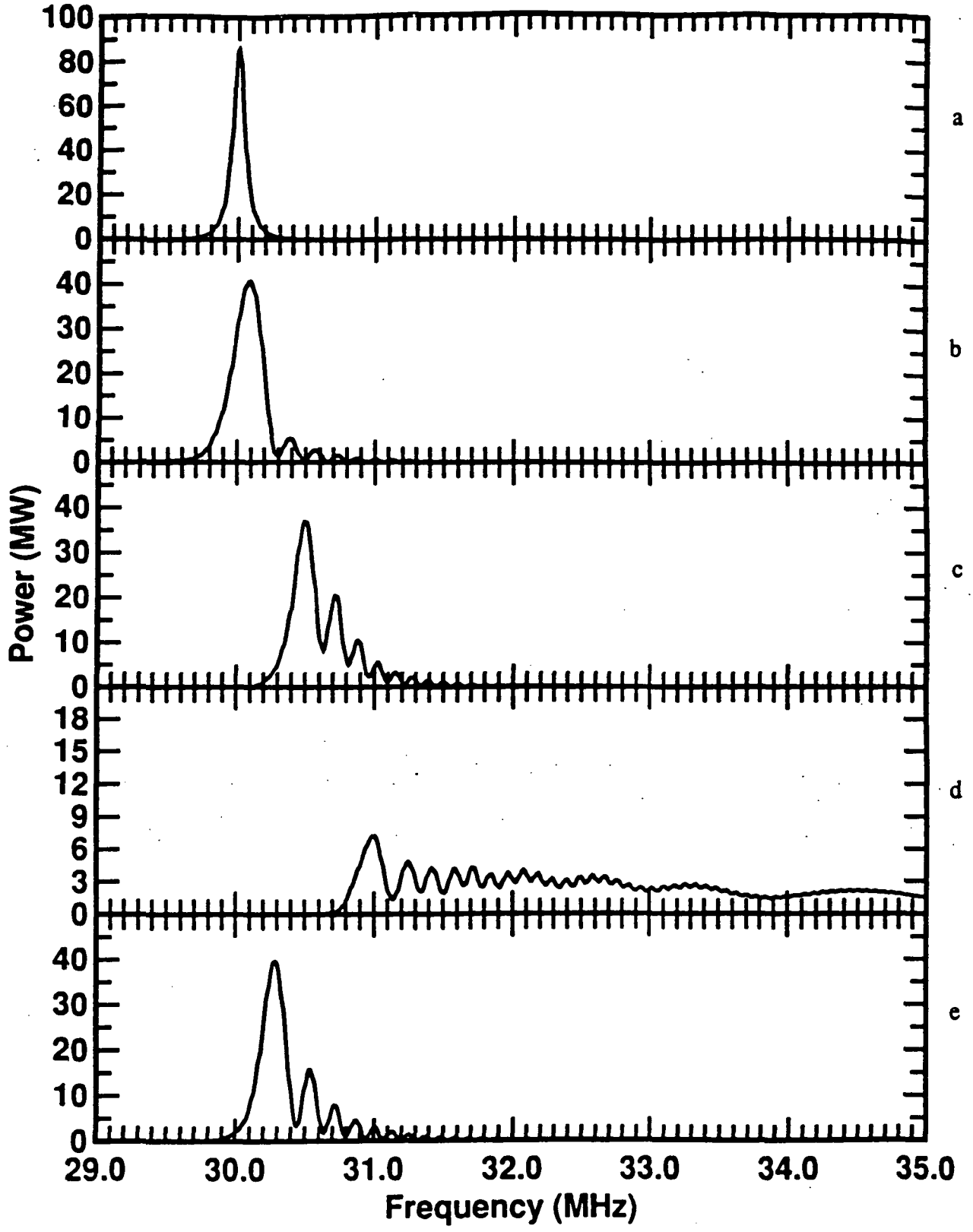

Figure (1.4) The power spectral density plots for (a) a chirp free laser and (b)-(e) the four different laser pulses discussed in the text.

PSD	Contains LIMP Chirp?	Contains Plasma Chirp?	Energy in a 300 kHz bandwidth about the peak.
Figure (1.4)a	No	No	17.9 J
Figure (1.4)b	Yes	No	15.1 J
Figure (1.4)c	Yes	Yes, $N_e^{pk} = 10^{12}$ cm^{-3}, $\tau_d = 2\,\mu s$	11.6 J
Figure (1.4)d	Yes	Yes, $N_e^{pk} = 5 \times 10^{12}$ cm^{-3}, $\tau_d = 2\,\mu s$	2.4 J
Figure (1.4)e	Yes	Yes, $N_e^{pk} = 10^{12}$ cm^{-3}, $\tau_d = 1\,\mu s$	12.6 J

Table (1.1)Pulse energy in a 300 kHz bandwidth.

Two possible methods of reducing the effect of the plasma chirp on the laser pulse spectrum are:

1. Ensure completion of the discharge pulse and the decay of the electron density prior to the start of the pulse. This can be aaccomplished using a short discharge pulse.
2. Use the fact that the LIMP and plasma frequency chirps sweep in opposite directions to offset each other. This is illustrated for the frequency chirps in Figure (1.3)b and Figure (1.3)d which are identical except for the plasma chirp decay time. Refering to Table (1.1) it can be seen that the longer plasma chirp decay of Figure (1.3)d offsets some of the LIMP frequency chirp resulting in more of the pulse energy in the required bandwidth.

1.6 Comparison with Experimental Results

The model detailed above is only of use if it can be validated against experimental results. Unfortunately most of the frequency chirp results published in the literature fail to provide all of the information necessary to construct the model. The laser at NOAA has been extensively characerised [1.14] and this was used as one point of comparison, whilst the measurements taken by the author during the LAWS laser breadboard testing (Section 2.0) provided the possibility of additional comparisons.

1.6.1 Comparison with the NOAA Laser.

Parameters for the NOAA laser were obtained from reference [1.14] and from discussions with M.J. Post of NOAA. Table (1.2) lists the parameter values used. in the model.

Parameter	Value	Parameter	Value
τ_{rise} (μs)	0.1	l (m)	0.6
τ_{relax} (μs)	2.2	σ (cm)	1.3
FWHM (μs)	1.5	λ (μm)	10.6
I_r	2	E (J)	0.73
$N_e pk$ (cm^{-3})	1.1×10^{12}	CO_2:N_2:He	2:1:7
τ_d (μs)	1	K (m^3kg^{-1})	2.055×10^{-4}
L (m)	3.1	ν_0 (THz)	41.7

Table (1.2) Parameter values used to model the NOAA laser.

Figure (1.5) shows the optical pulse from the NOAA laser and Figure (1.6) shows the optical pulse and optical pulse energy as a function of time for the model. It can be seen that no attempt

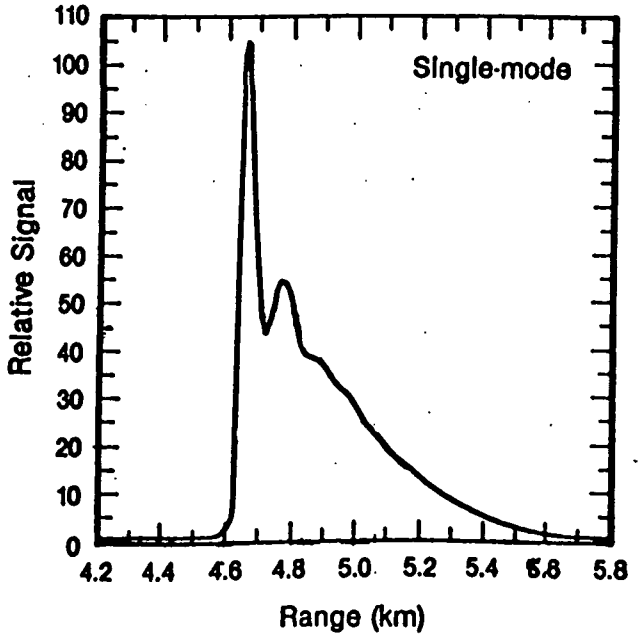

Figure (1.5) The output pulse from the NOAA laser (from reference [1.14]).

was made to model the relaxation oscillation after the gain switched spike and that an approxima-

tionof a mean intenslty through this portion of the pulse was used. This is satisfactory as the effect of this on the frequency spectrum will be small.

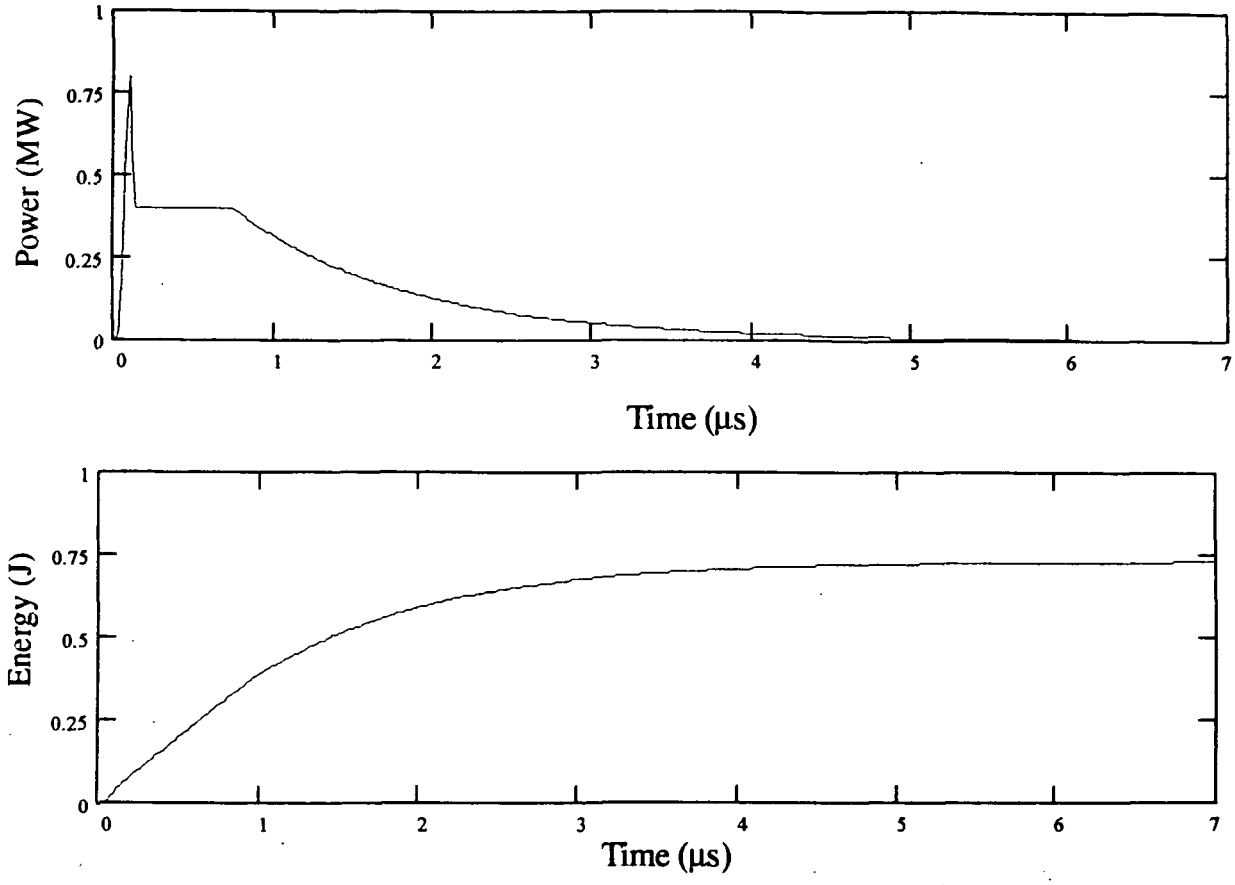

Figure (1.6) The optical pulse shape and energy evolution for the model of the NOAA pulse.

Figure (1.7) (lower trace) shows the measured frequency chirp from the NOAA device. and

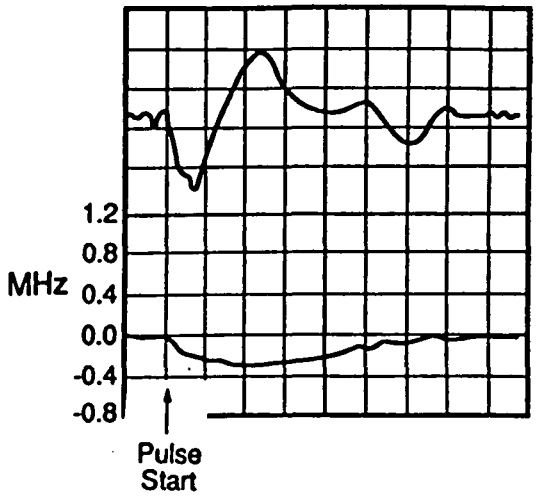

Figure (1.7) The measured frequency chirp (lower trace) from the NOAA device. Horizontal scale is 1 μs/division (From reference [1.14]).

Figure (1.8) shows the calculated frequency chirp and pulse spectrum. It can be seen that there is

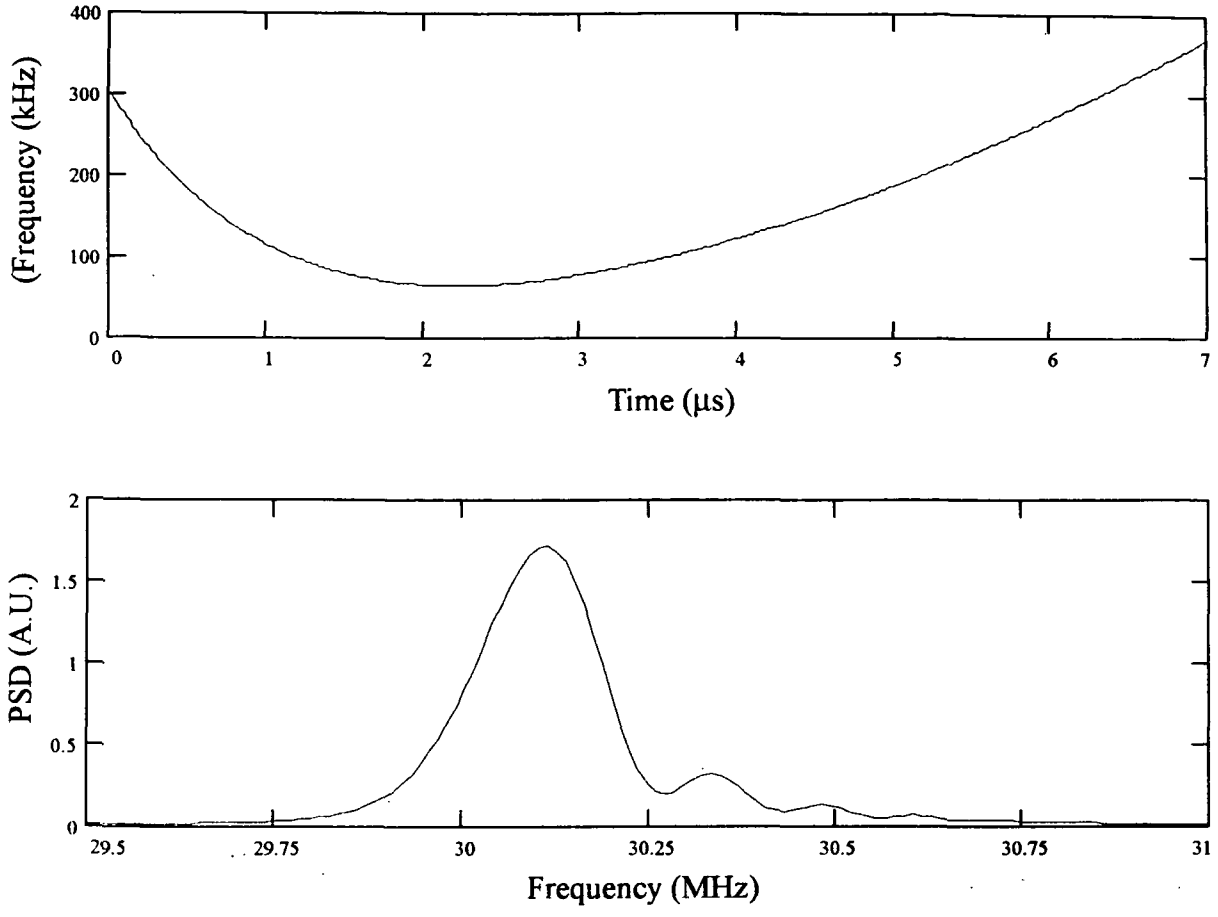

Figure (1.8) The model results for the frequency chirp as a function of time and the power spectral density of the NOAA laser.

close agreement between the experiment and theory for the time dependent frequency chirp. It should be noted that the calculation of frequency chirp in reference [1.14] is in error. Although a power spectral density plot is not provided in the paper, a histogram of returns from a hard target is provided (1 m/s ~200 kHz). It can be seen that the general shape and width of the histogram reflects the shape of the power spectral density function as might be expected.

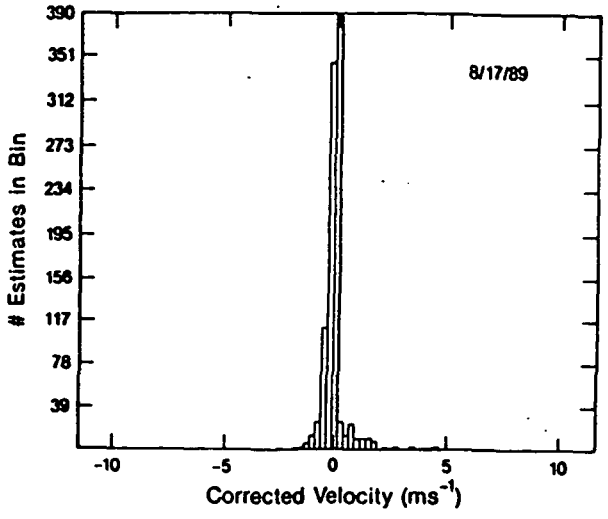

Figure (1.9) A histogram of returns from a hard target using the NOAA lidar The velocity can be converted to frequency using the approximation that 1m/s ~ 200 kHz. (From reference [1.14]).

1.6.2 Comparison with the STI Optronics LAWS Breadboard.

Section 2.3 details the STI Optronics breadboard performance and Appendix 2 contains the data collected. The pulse shape, energy evolution as a function of time and frequency spectrum are shown on pages A2.6, A2.7, A2.9 and A2.10 respectively. As detailed in Section 2.3.2.3 it was not possible to determine the frequency as a function of time. Table (1.3) lists the model parameters

Parameter	Value	Parameter	Value
τ_{rise} (μs)	0.2	l (m)	1.4
τ_{relax} (μs)	3	σ (cm)	2.1
FWHM (μs)	2.5	λ (μm)	10.6
I_r	2	E (J)	2.6
$N_e$pk (cm^{-3})	5×10^{11}	CO_2:N_2:He:H_2	5:10:4:1
τ_d (μs)	1	K (m^{3}kg^{-1})	2.179×10^{-4}
L (m)	5.1	ν_0 (THz)	41.7

Table (1.3)Parameter values used to model the STI Optronics LAWS breadboard laser.

used to model the STI device. The parameters were derived from the measurements made. An average intensity approximation was used for the relaxation oscillations which occur in the intensity profile immediately after the gain switched spike. Comparison of the time dependent energy evolution from the model (Figure (1.10)) with the experimental result (page A2.7) shows close agreement.

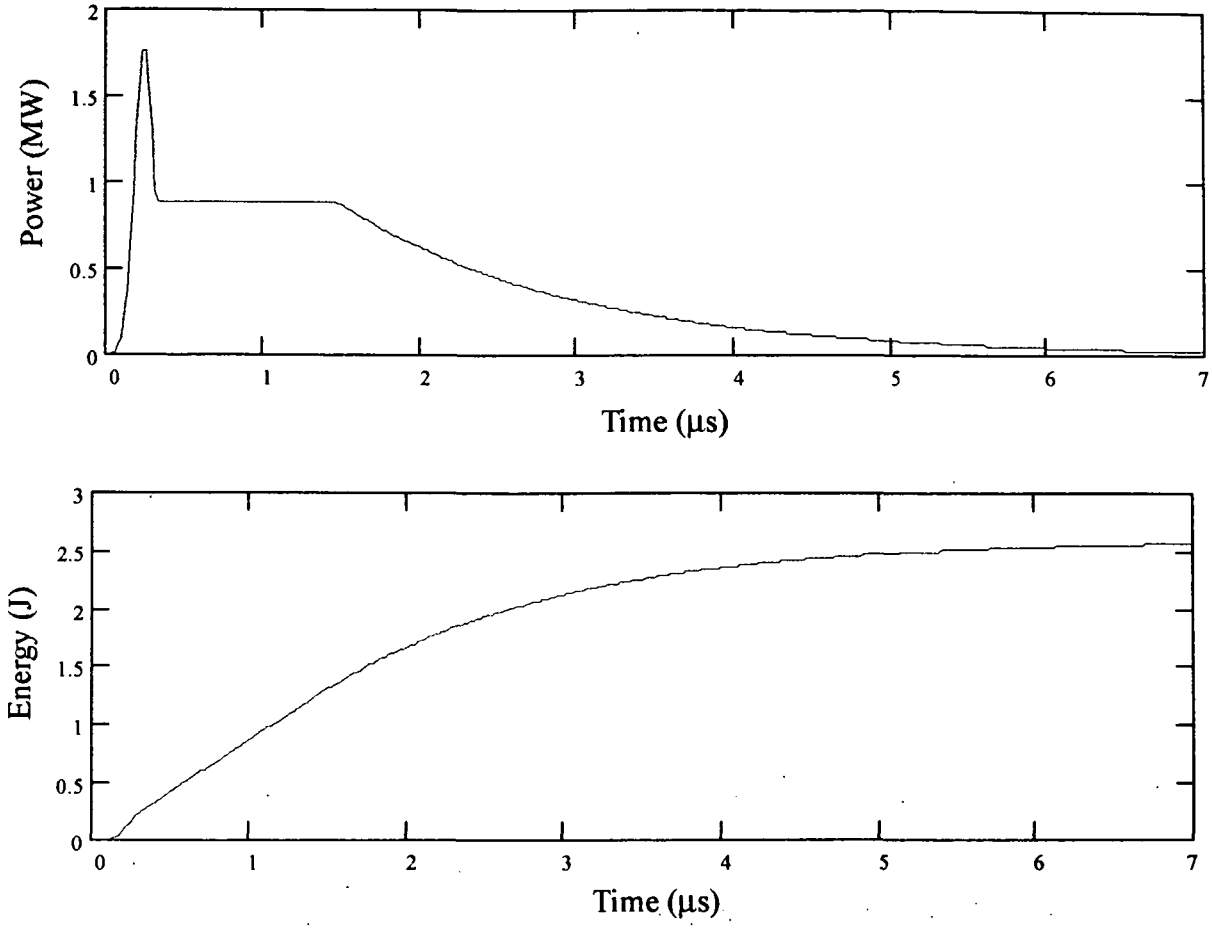

Figure (1.10) The optical pulse shape and energy evolution for the model of the STI pulse.

Figure (1.11) shows the time dependent frequency chirp and pulse spectral density from the model. Comparison of the model results with the experimental results (pages A2.9 and A2.10) show general agreement with both having a FWHM of ~200 kHz. The experimental result has more energy in the oscillations on the high frequency side of the main spectral peak. This may be due to the transverse mode beating exhibited by the pulse (Section 2.3.2).

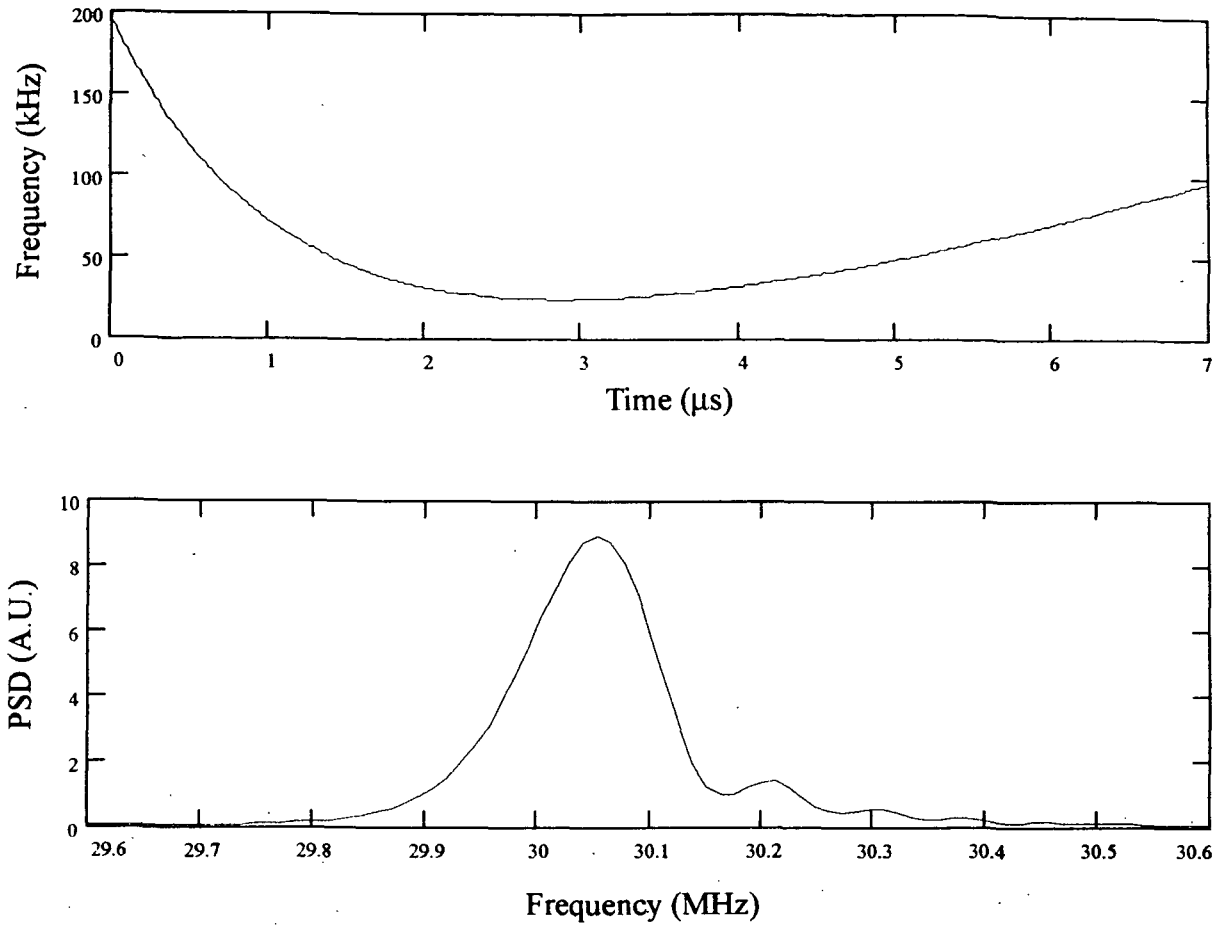

Figure (1.11) The model results for the frequency chirp as a function of time and the power spectral density of the STI laser.

1.6.3 Comparison with the Textron Defense Systems LAWS Breadboard.

Due to the difficulty in collecting reliable experimental data (Section 2.2.1), only a detailed comparison of the model with the TDS model. Pages A1.7 and A1.8 show the measured and calculated frequency chirp for the device. These results and their accuracy are discussed in Section 2.2.2.3.

1.7 Summary

A flexible model of the frequency chirp in pulsed CO_2 lasers has been developed to allow the frequency chirp effect of various basic laser parameters to be investigated. The model was compared with experimental results from the NOAAlaser and the LAWS laser breadboards. There was excellent agreement with the NOAA device and good agreement with the LAWS laser breadboards, the quality of the data from these devices providing the limitation on the comparison.

1.8 References

[1.1]W.A. Stiehl and P.W. Hoff, Appl. Phys. Lett., **22**, 680 (1973).

[1.2]J.A. Weiss and J.M. Schnur, Appl. Phys. Lett., **22**, 453 (1973).

[1.3]P. Pace and M. Lacombe, Can. J. Phys., **57**, 1350 (1979).

[1.4]P. Pace and M. Lacombe, Opt. Commun., **26**, 405 (1978).

[1.5]J.-L. Lachambre, P. Lavigne, M. Verreault and G.Otis, IEEE J. Quant. Electron., **QE-14**, 170 (1978).

[1.6]P.W. Pace and J.M. Cruickshank, IEEE J. Quant. Electron., **QE-16**, 937 (1980).

[1.7]W.M. Lipchak, Opt. Commun., **19**, 205 (1976).

[1.8]D.V. Willetts and M.R. Harris, J. Phys. D.: Appl. Phys., **15**, 51 (1982).

[1.9]M.R. Harris and D.V. Willetts, J. Phys. D: Appl. Phys., **16**, 125 (1983).

[1.10]D.V. Willetts and M.R. Harris, IEEE J. Quant. Electron., **QE-19**, 810 (1983).

[1.11]D.V. Willetts and M.R. Harris, Appl. Phys. B, **33**, 91 (1984).

[1.12]S. De Silvestri, P. Laporta, V. Magni and O. Svelto, IEEE J. Quant. Electron., **QE-24**, 1172 (1988).

[1.13]C.J. Elliot, O.P. Judd, A.M. Lockett and S.D. Rockwood, Los Alamos Lab. Report LA-5562-MS (1974).

[1.14]M.J. Post and R.E. Cupp, Appl. Opt., 29, 28, 4145 (1990).

2.0 LAWS Laser Breadboard Results

This section contains information provided by the LAWS laser breadboard contractors which they may regard as competition sensitive.

2.1 Introduction

Towards the end of the LAWS laser breadboard contracts, we visited both of the laser contractors (STI Optronics and Textron Defense Systems) to measure the performance of each of the laser breadboards. The contractors were free to choose a date for the visit. The intention was to acquire data using a digital oscilloscope so that it could be analysed. STI Optronics had a suitable digital oscilloscope whilst NASA MSFC supplied a digital oscilloscope to Textron Defense Systems for our use.

It should be emphasised that during short duration visits, such as those undertaken here, it is only possible to obtain a snapshot of each laser's performance. This chapter summarises the impressions and findings of the visits, data from the visits is provided in Appendices 1 and 2.

2.1.1 Measurements Made

Table (2.1) lists the parameters measured or obtained from the contractors during the visits.

Parameter	Obtained from
Discharge voltage pulse shape	Measurement
Discharge current pulse shape	Measurement
Optical pulse energy	Measurement
Optical pulse shape	Measurement
Heterodyne beat signal	Measurement
Storage capacitor charging voltage	Measurement / Contractor information
Storage capacitance	Contractor

Table (2.1) Parameters measured.

The only method of determining beam profiles at both contractors was to place thermal paper in the beam path to obtain a burn pattern. Whilst this method gives a 'feel' for the beam profile it is not very quantitative. Neither contractor had an accurate means of measuring beam quality or beam jitter at the time of visiting.

The voltage and current pulse profiles are particularly important for analysing the data from the breadboards. Integrating the voltage and current pulses as a function of time enables both the total energy and the energy deposited into the discharge to be calculated as a function of time. The efficiency of the laser is strongly dependent on the reduced electric field, E/N(t) at which the energy

is deposited into the discharge. For each laser, the reduced electric field as a function of time was calculated from the discharge voltage pulse. This is simply given by:

$$E/N(t) = \frac{V(t)}{dN} \tag{2.1}$$

where V(t) is the time varying discharge voltage, d is the discharge electrode separation and N is the gas molecular number density. Plotting the energy deposited into the discharge as a function of the value of the reduced electric field provides a good indication of how well the discharge circuit has been optimised.

The energy stored in the pulse forming network can be calculated from the storage capacitance and the charging voltage. The capacitance of the pulse forming network was obtained from each of the contractors. The ratio of the discharge energy to the stored energy gives the efficiency of the pulse forming network. The ratio of the optical pulse energy to the energy deposited in the discharge is the intrinsic efficiency of the laser. Dividing the voltage by the current provides a value for the discharge impedance which can be used to optimise the design of the pulse forming network.

For a particular gas mixture, the electron drift velocity can be determined as a function of the reduced electric field (Section 1.3.2) and the electron number density determined (equations (1.22) and (1.23)). Once the electron number density has been determined, the frequency chirp during the optical pulse can be modeled (Section 1).

It is important that the recording device be triggered from a reliable and consistent source, such as the discharge circuit trigger, so that accurate timing between the voltage, current and optical pulses is maintained. If this is not done, the analysis detailed above can not be completed accurately. At both of the contractors visited, the oscilloscope used to capture the results was a dual channel device. The second channel was used to monitor the discharge current pulse such that every piece of data could be referenced to the start of the current pulse.

2.2 Textron Defense Systems

Textron Defense Systems (TDS) is the laser sub-contractor for Lockheed Missile and Space Company (LMSC) and they were visited on May 27th - 29th 1992. All measurements were carried out using a 1:1:3 $C^{16}O_2$:N_2:He gas mixture at a total pressure of 340 torr and a laser pulse rate of 1 Hz unless otherwise stated.

2.2.1 General Comments

The laser was obviously not complete at the time of this visit. Evidence of this was the temporary high voltage feedthroughs on the laser head, a somewhat untidy arrangement of signal and data cables, and no evidence of autonomous operation ability - everything was adjusted by hand.

The output pulse energy from the laser was reduced by a beam splitter and measured using a joule meter. The surface of this energy meter was damaged (from previous work) and the contractor indicated that the detector underestimated the output energy by ~5 % if the manufacturer's calibration was used, which was the case for all the results detailed here (it was not possible to independently verify the calibration in the short time available). The beamsplitter permitted 3% of the output energy to fall on the detector. This was verified by removing the beam splitter at low pulse energies and then replacing it.

The contractor indicated that the pulse forming network capacitance was 410.8 nF and that charging voltages in the 18 kV - 21 kV would be used during testing. This is below the original specification of the device and was limited by insulation and preioniser problems. During preliminary testing of the preioniser material the contractor discovered that occlusions in the material prevented the full design voltage from being placed across the material. The short time schedules and limited budget for the development of the laser precluded going back to the material manufacturer and screening material (using x-rays or ultra-sound) to obtain defect free material. The laser was therefore assembled using potentially flawed preionisers and a decision made (by the contractor) to restrict the loading across the preioniser. In any future development the contractor would replace the preionisers with suitably screened material.

On the first day, during initial operation of the laser, one of the preioniser high voltage cables punctured. This occurred before any measurements could be taken. Several temporary fixes were attempted by the contractor before it was decided that the laser chamber would have to be opened to the atmosphere so that a permanent repair could be carried out. This provided an opportunity to examine the construction of the laser head - this appeared to be well designed and manufactured internally, in contrast to the temporary nature of the high voltage feedthroughs on the outside of the laser head. After completing the repairs the laser operated without breakdown of the cables for the remainder of the visit, however a whole day was lost because of this failure. Since this visit the contractor has installed more robust high voltage feeds on the laser head.

Considerable electromagnetic interference (EMI) from the laser prevented the NASA supplied digital oscilloscope from operating properly and an oscilloscope camera and analog oscilloscope were used to acquire the data. The traces on the photographs were then 'hand digitised' to provide numerical data for analysis (Appendix 1). This is obviously unsatisfactory but enabled the data to

be collected. There were several potential sources for this EMI - the most likely being the temporary high voltage feedthroughs.

2.2.2 Performance

Data sets were collected using the oscilloscope camera for laser pulse forming network charging voltages of 18 kV, 19 kV, 20 kV and 21 kV

2.2.2.1 Output Pulse Energy, Intensity Profile and Efficiency.

Table (2.2) summarises the single mode output pulse energies measured. All of these are below the design specification, as would be expected with the laser being operated below it's design point. The optical output pulse profile is shown on page A1.6 for two different detectors. The optical output pulse started 2 μs into the discharge pulse. It was noticed that the output pulse energy for a given charging voltage varied for different gas fills, although it was constant for any particular fill.

Charging Voltage (kV)	Stored Energy (J)	SLM Output Pulse Energy (J)	Efficiency (Estore/Eout) (%)
18	66.6	3.3	5.0
19	74.1	4.3	5.8
20	82.2	5.8	7.1
21	90.6	7.8	7.8

Table (2.2)A summary of the single mode output pulse energies obtained from the TDS Breadboard.

It can be seen Table (2.2) that as the energy loading on the discharge increases towards the original design point, the efficiency increases to ~8 %, close to the intrinsic efficiency design point of 9 % even without consideration of the pulse forming network transfer efficiency. At a charging voltage of 18 kV integrating the discharge current and voltage (page A1.3) gives a deposited energy of 61.7 J into the discharge. This corresponds to a pulse forming network to discharge transfer efficiency of ~92 %. The intrinsic efficiency of the laser at this charging voltage is ~5.4 %. This low intrinsic efficiency can be accounted for by noting that a lot of the discharge energy is deposited at higher than ideal values of the reduced electric field, E/N (page A1.5). It should be noted that gaps in this figure are a consequence of the poor resolution of the data collection technique.

The pulse has a nominal length of 4 μs (FWHM, ignoring the gain switched spike) which is longer than the required pulse. At the time of this visit the contractor had not completed optimisation of the pulse forming network and it was anticipated that the pulse length would be reduced

when this is done. One of the reasons for this may be the assumption of an ~8 Ω discharge impedance whilst the actual value is closer to ~30 Ω (page A1.4).

2.2.2.2 Single Mode Performance

The laser was injection locked through one of the resonator fold mirrors by a c.w. CO_2 oscillator. Injection matching electronics were used to match the cavity length to the injection frequency prior to the optical discharge. This cavity match was provided with an offset to compensate for the cavity length change due to the discharge plasma (Section 1.3.2). This was not an active compensation but a passive one to ensure cavity length matching at the start of the optical pulse. As the discharge conditions were varied (changing the charging voltage), this offset had to be adjusted manually.

To determine if single mode operation was occurring, the optical pulse shape was monitored on an oscilloscope. When single mode operation was not present, mode beating could be seen in the pulse envelope as a high frequency modulation of the pulse shape. When first turned on at the low charging voltage (18 kV), the laser had difficulty obtaining single mode operation. After 5 minutes of operation the single mode performance had stabilised so that ~60% of the pulses were single mode. As the charging voltage was increased the reliability of the single mode operation decreased, down to less than 10% of the pulses at the 21 kV charging voltage.

The contractor expressed concern that the single mode performance had been better than this (~100% single mode at 18 kV) prior to the visit. It was suggested, by the contractor, that the alignment of the laser discharge chamber with the laser resonator was not quite correct. The laser chamber had to be moved out from the laser resonator to repair the high voltage cable failure and then replaced in the same location as prior to the repair. A relatively large and bulky item such as this does not move especially smoothly on castors and aligning it with the resonator can be frustrating! Since the visit the contractor has implemented a mechanical alignment scheme to assist in repositioning the laser head in such circumstances.

2.2.2.3 Frequency Chirp / Frequency Spectrum

This was the hardest of the performance parameters to assess because of the data collection method. In order to determine the frequency chirp, multiple oscilloscope photographs were taken, each of one section of the heterodyne beat signal. These were 'hand digitised' using a graduated scale to provide numerical values to feed into the analysis program. Although data was collected for several charging voltages, on examination of the data after the visit, it was determined that only the 18 kV set was unambiguous as to the location of the 'join points' between the several photographic records required for each measurement. The frequency chirp measured on the device is shown on page A1.7 together with the optical pulse. It can be seen that there is a frequency chirp of (800 ±200) kHz after ~3 μs. The large errors on the data reflect the quality of the data collection method. Most of this is probably due to plasma chirp during the discharge decay and page A1.8 shows the results of a calculation of the plasma chirp made using the voltage and current pulses (pages A1.1 and A1.2). It can be seen that the magnitude of the plasma chirp is in agreement with the measured value but the rise time of the two plots is considerably different. Without better data, further analysis is pointless.

2.2.2.4 Operation at High Pulse Rates

High pulse rate operation was demonstrated at the 19 kV charging voltage with a multimode output. The contractor was extremely cautious in increasing the pulse rate. The laser design uses a pair of fans to provide redundancy in the final system. As the pulse rate is increased the fan speed must be increased to maintain gas flow clearance through the discharge region between pulses. Each fan was controlled separately, requiring a different rotation speed for a given gas flow velocity. If the speeds of the fans are incorrectly adjusted, a standing wave is set up in the gas loop resulting in a beat note sound which is shortly followed by a loud squealing from the fans. This was experienced during the visit. Within a month or two of this visit one of the fans in the laser seized and failed as a consequence of this standing wave pattern. To accurately control the fan speeds over a long period of time would require a sensor unit and control mechanism so that changes in fan characteristics over time could be compensated for.

The laser was operated at pulse rates of 10 Hz for 75 s, 12.5 Hz for 120 s, 14.7 Hz for 120 s and 19.5 Hz for 195 s. The period of operation was limited by overheating of resistors in the pulse forming network. The discharge appeared to be uniform at all pulse rates (and through out the visit) and no arcs were noticed except for the period when the standing wave started to establish itself. When the fan speeds were readjusted to eliminate the beat note, the arcing stopped. The output power at each of the pulse rates was 52 W, 63 W, 73 W and 100 W respectively. This is an approximately linear progression (5.2, 5.0, 5.0 and 5.1 J/pulse respectively) indicating no discernible fall off of energy with pulse rate.

2.3 STI Optronics

STI Optronics (STI) is the laser sub-contractor for General Electric (GE) and they were visited on September 15th - 17th 1992. All measurements were carried out using a 5:2:1:4 $C^{16}O_2$:N_2:H_2:He gas mixture at a total pressure of 200 torr and a laser pulse rate of 0.5 Hz unless otherwise stated. Rex Geveden of NASA MSFC and M.J. Post of NOAA also visited the contractor.

2.3.1 General Comments

Prior to visiting the contractor we were supplied with a copy of an analysis of the laser's frequency spectrum carried out by the contractor. We determined that the contractor was not measuring the laser spectrum. The contractor was using a single local oscillator for both heterodyne detection and injection locking (Figure (2.1)). The beam from the local oscillator was split, one portion going to the heterodyne detector, the other portion was passed through an acousto-optic modulator and frequency shifted by 30 MHz prior to injection into the laser resonator off the grating.

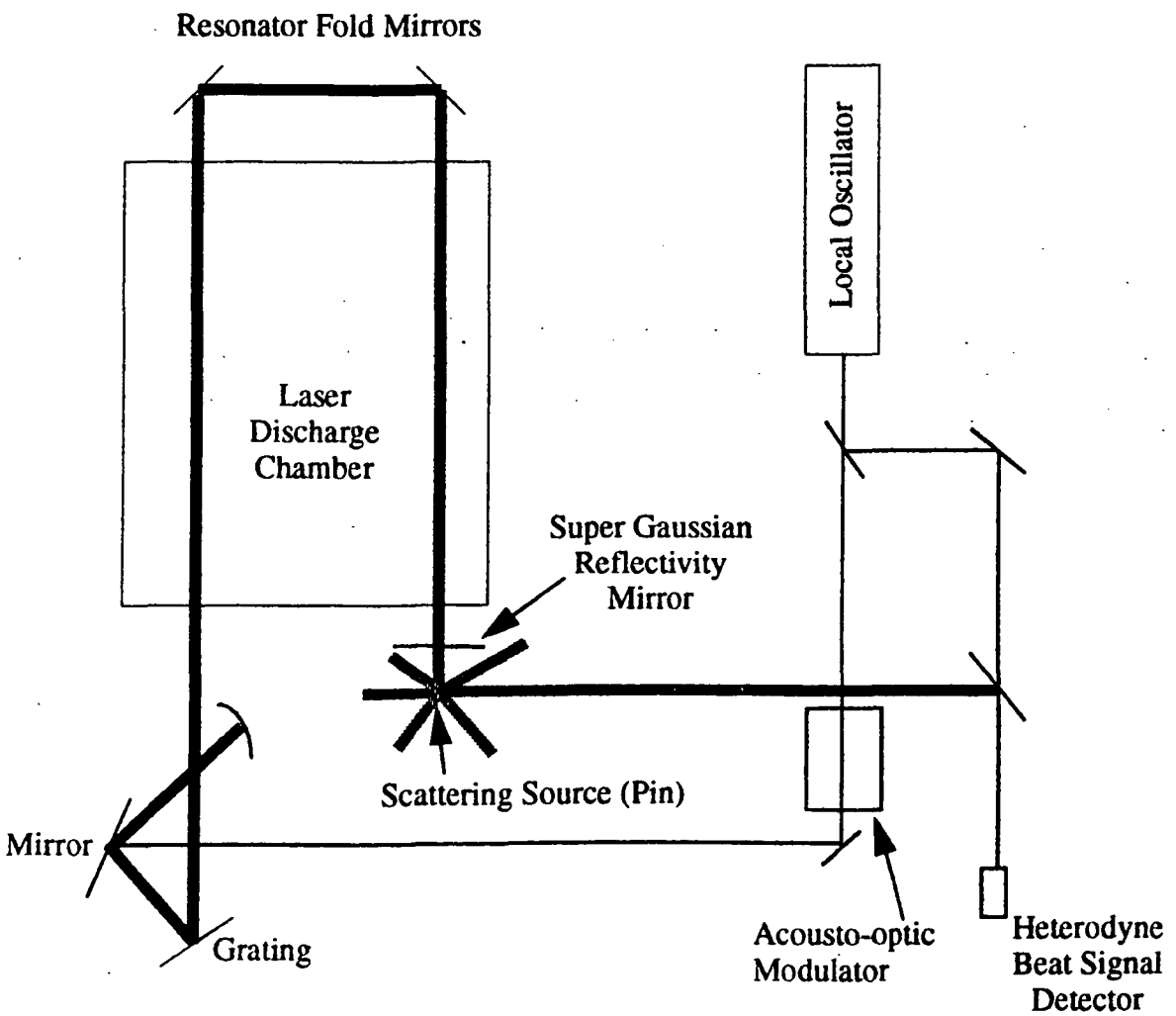

Figure (2.1) STI Optronics injection scheme and heterodyne detection arrangement.

If the local oscillator is at a frequency f MHz then the laser is at a nominal frequency of f + 30 MHz (assuming the injection seeding is successful). It was determined that even with the local oscillator blocked from the heterodyne detector, a heterodyne signal was seen. It was deduced that this signal was between the laser and the laser + 30 MHz signals i.e. between f+30 MHz and f + 60 MHz. This occurred because of feedback from the laser through the acousto-optic modulator (producing the f + 60 MHz signal). To permit the frequency spectrum of the laser to be determined, the scattering source (pin) was removed so that only the local oscillator and local oscillator + 60 MHz signals fell on the detector. Although not an ideal arrangement, this did permit the laser frequency spectrum to be measured.

The contractor indicated that the laser discharge was much wider (~8 cm) than designed (5 cm) and that a consequence of this was that the gain was not highest on the center of the discharge. Obtaining a wider discharge than anticipated is not a problem typically encountered in pulsed TE CO_2 lasers and is indicative of the very high preionisation levels achieved by this device. Two approaches could be used to reduce the discharge width. The first would be to modify the discharge circuit to reduce the time delay between the preionisation and main discharge pulses. This would reduce the distance over which the preionising electrons could diffuse. The second approach would be to narrow the preioniser width. The contractor indicated that the laser discharge circuitry had not been optimised.

The laser required one person to operate it. All the basic control parameters - discharge voltage, pulse rate and injection lock loops could be controlled by the operator from a touch panel screen. Filling the laser with gas and adjusting the resonator cavity (with the exception of the injection lock control) were still manual operations.

The contractor indicated that the laser head had a slow leak which had not yet been located.

2.3.2 Performance

Data sets were collected at pulse forming network charging voltages of 22.5 kV and 26.5 kV. Data was collected using a dual channel 500 Msample/s/channel digital oscilloscope. Heterodyne beat signal data was also collected at a 1 GHz sample rate on a single channel. The data was transferred to floppy disk for analysis after the visit. Laser pulse energies were measured at additional charging voltages as indicated in the text.

2.3.2.1 Output Pulse Energy, Intensity Profile and Efficiency.

The contractor indicated that the storage capacitance was 400 nF. Table (2.3) summarises the sin-

Charging Voltage (kV)	Stored Energy (J)	SLM Output Pulse Energy (J)	Efficiency (Estore/Eout) (%)
22.5	101.25	2.6	2.6
26.5	140.45	7.1	5.1
28.5	162.45	7.7	4.7
30.5	186.05	8.3	4.5

Table (2.3)A summary of the single mode output pulse energies obtained from the STI Breadboard.

gle mode output pulse energies obtained. The contractor was unhappy with the discharge width and non-uniform gain distribution, which reduced the available single mode energy considerably. When the laser was allowed to run multimode, the energy at the 22.5 kV charging voltage increased to 7.1 J (resulting in an efficiency of ~7.6 %). Whilst an increase in energy is normally expected in going from single to multimode operation this is a surprisingly large increase.

The contractor was also concerned that operating at 10.6 μm with optics optimised for 9.11 μm operation would also decrease the laser efficiency. He was particularly concerned about diffraction grating losses. To demonstrate this he positioned a mirror in front of the grating to demonstrate the increased multimode output (Table (2.4)). Finally to demonstrate maximum energy

Charging Voltage (kV)	Stored Energy (J)	Multimode Output Pulse Energy (J)	Efficiency (Estore/Eout) (%)
22.5	101.25	9	8.8
26.5	140.45	13.6	9.7
28.5	162.45	15.2	9.4
30.5	186.05	17.1	9.2

Table (2.4)A summary of the multimode output pulse energies obtained from the STI Breadboard when the grating was replaced with a mirror.

extraction from the laser the contractor replaced the super-Gaussian reflectivity mirror with a 10 m radius of curvature 55 % reflectivity output coupler to form a stable resonator. This enabled an output energy of 20.7 J (multimode) to be extracted at the 30.5 kV charging voltage.

The object of these demonstrations by the contractor was to show that the required energy existed in the gain medium and that, in his opinion, it was only necessary to optimise the resonator to extract it. The contractor also indicated a desire to change the injection scheme to one similar to that used by TDS in an effort to further improve efficiency.

It should be noted that integration of the current and voltage pulses (page A2.1 - A2.3) gives the energy deposited into the discharge as 114.7 J, compared to a calculated stored energy of 101.25 J. This is the difference between using a charging voltage of 22.5 kV and 24 kV which is considerable. This difference was only discovered after the visit during analysis and there is insufficient information to resolve the discrepancy. There are several potential sources of this difference - slight saturation of the voltage monitor at the start of the discharge pulse and an incorrectly calibrated voltage source/voltage probe or current probe for example. Using this value for the energy deposited into the discharge gives an intrinsic efficiency of 2.3 % at the 22.5 kV voltage. The discharge impedance was found to be ~30 Ω. The energy is deposited at high values of the reduced electric field (page A2.5) which will also reduce the efficiency. As mentioned previously, the contractor had conducted no optimisation of the pulse forming network.

The output pulse profile is shown on page A2.6. The pulse length is ~2.5 μs (FWHM ignoring the gain switched spike) which is shorter than the desired 3 μs.

2.3.2.2 Single Mode Performance

The non-uniform gain in the discharge made it difficult to achieve single mode operation. At the 22.5 kV charging voltage single mode operation, determined by monitoring the pulse intensity profile), appeared to be very reliable (~100 %), once it had been obtained. This was achieved at a considerable efficiency penalty as indicated in the previous section. To obtain single mode operation the contractor had to use an aperture stop to restrict the region of gain used; thus effectively throwing away energy. Until the discharge width is reduced there does not appear to be a simple means of overcoming this problem. It should be noted that subsequent analysis of the heterodyne beat signal showed the presence of transverse mode beating, which was not noticed at the time the data was collected, indicating that single mode operation may be less reliable than originally anticipated. Single mode operation at higher charging voltages was extremely difficult to achieve and maintain.

2.3.2.3 Frequency Chirp / Frequency Spectrum

The heterodyne beat signal obtained at a charging voltage of 22.5 kV is shown on page A2.8 and the power spectral density plot is shown on pages A2.9 - A2.10. It can be seen that at this pulse energy the laser has a spectral width (FWHM) of ~200 kHz. From page A2.8 it can be seen that the laser signal was much larger than the local oscillator signal. Whilst it was possible to obtain frequency spectrum (A2.9 - A2.10) for the pulse, the algorithms developed to measure the frequency as a function of time did not work adequately as they look for zero crossing points in the beat signal. A high pass digital filter did not adequately remove the pulse envelope to allow the algorithm to be used. The ad-hoc nature of the measurement and the short time period available made attenuation of the laser signal impractical at the time data was collected.

Careful examination of page A2.8 indicates digitiser saturation during the gain switched spike, potential mode beating ~1 μs into the pulse and ~6.5 μs into the pulse. The mode beating at t = 3 μs (~1 μs into the optical pulse) is shown on page A2.11. The beat period is ~0.2 μs indicating that this is probably transverse mode beating.

All the data collected at the 26.5 kV voltage was found to be contaminated by both axial and transverse mode beating and is not shown here.

2.3.2.4 Operation at High Pulse Rates

The contractor had not performed any flow loop optimisation and only brief operation at pulse rates up to 5 Hz was demonstrated. He indicated that the flow from the fan was non-uniform, requiring the repositioning of the diffuser vanes which would require disassembly of the laser head.

2.4 Summary and Conclusions

As the previous discussion of results has made clear, visiting for a day or two and acquiring data for subsequent analysis is not capable of adequately characterising the performance of each device. Any future effort along these lines should occupy at least a week at each contractor so that a more thorough examination of each device could be conducted. This would also permit preliminary data analysis on sight so that any anomalies could be re-examined.

Putting aside the discharge problems encountered by both contractors, for which there appears to be perfectly reasonable solutions, the pulse length, pulse energy and efficiency are achievable. The two outstanding uncertainties, of the parameters measured, in the performance of the breadboards are the demonstration of reliable single mode operation at the energies required from this device and the achievement of the frequency spectrum requirement. Both contractors exhibited increasing difficulty in achieving single mode operation as the output energy was increased, despite using different resonator configurations and injection geometries. The frequency spectrum data was inconclusive because of the inability to achieve the required pulse energies.

Any future work should ensure that the contractors have a quantitative method of measuring the beam profile, beam quality and beam jitter to the accuracies required by the specification.

At the completion of these visits we formed the impression that these two teams were complimentary and would form a much stronger team in cooperation rather than competition with each other. This is obviously unlikely to happen and we feel that given adequate time and resources either team would be able to complete the breadboard development on their own.

In developing complex, highly stable lasers, as these breadboards were intended to be, it is always prudent to allow time and resources to parameterise and optimise the laser performance. Both contractors were so constrained by time that no sooner were the breadboards assembled than they had to be characterised for performance. Whilst not wishing to get into the issue of responsibility, it appears that too much was undertaken in too little time with too little money. It should be noted that both contractors put in considerable effort to overcome these limitations and achieve as much as possible within the time and fiscal constraints available.

3.0 LAWS Power Budget on a Spot MK2 Platform

3.1 Introduction

This chapter details a model of the power requirements of a low energy LAWS instrument on a Centre National D'Etudes Spatiales (CNES) supplied Spot MK2 platform. The Spot MK2 is being designed by Matra Marconi Space and will be available in various configurations. The platform will support payloads masses of 1.5 - 1.8 tonnes and is designed to have a 5 -7 year life. Solar arrays on the platform will provide between 2100 W and 3700 W of power.

3.2 Power System

The power system can be divided into two systems, those required by the spacecraft and the instrument systems.

3.2.1 Spacecraft Power

The data for the spacecraft side was provided by CNES. The initial Spot MK2 supplies 2100 W at an unregulated 22 - 37 Volts whilst later models will provide greater power. The spacecraft avionics and power distribution losses amount to ~400 W and for end of life calculations the power from the solar cells should be reduced by 10 %. There are four 40 A-hr batteries on the spacecraft for which charge/discharge efficiencies of ~86 % were assumed, based on information provided by NASA Marshall Space Flight Center.

3.2.2 Instrument Power

The instrument will consist of a low voltage regulator and convertor providing 120 V to the various sub-systems. These can be divided into systems required whilst the laser is firing and systems that require constant power (standby power). The standby power is ~ 540 W [3.1] assuming all systems except the laser pulse forming network require power. The laser pulse forming network is charged at high voltage (~20 - 30 kV) and a voltage converter is required to increase the 120 V line to the desired level.

The laser is assumed to be a 5 J CO_2 laser with an intrinsic efficiency of 9 % and a pulse forming network to discharge transfer efficiency of ~72 %, based on results from the LAWS laser breadboards. The laser is designed for a maximum pulse rate of 10 Hz.

Figure (3.1) shows a block diagram of the power system. The dimensionless numbers represent the efficiencies of each of the components. The power from the solar arrays has been represented as P W to allow this value to be varied. The overall power balance is determined by the orbit selected and by the laser pulse energy and firing duty cycle.

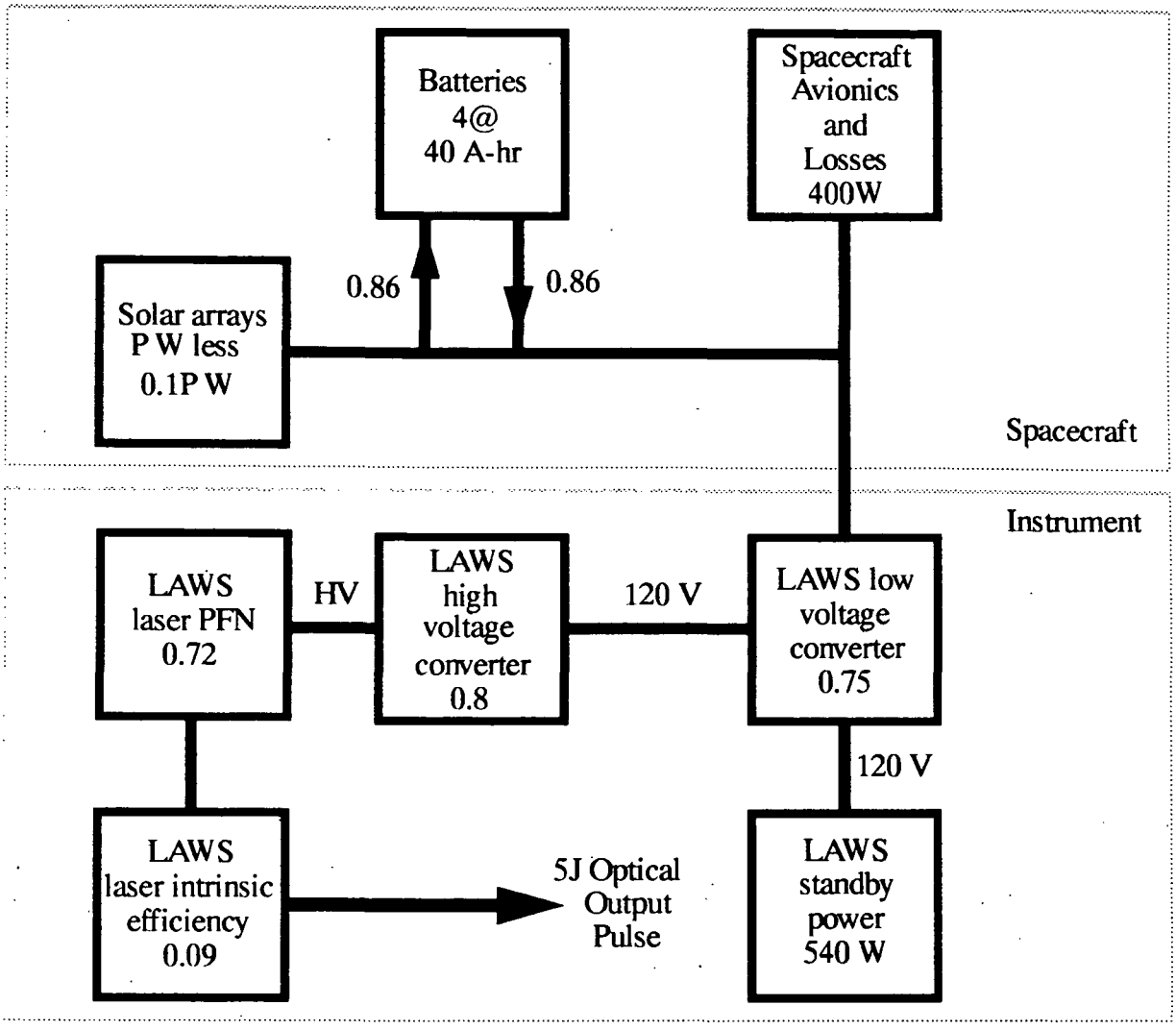

Figure (3.1) A block diagram of the power system for a 5 J LAWS instrument on a CNES Spot MK2 platform.

3.3 Orbit parameters

Only one orbit was considered by the NASA/CNES collaboration. This was a 525 km altitude, sun synchronous orbit. The sun synchronous orbit maximises the amount of time the satellite is in the sun and leads to an orbit inclination of ~98 degrees. As the earth orbits the sun, the satellite orbit will vary from an optimum of complete exposure to the sun to a worst case where ~22 minutes of the ~95 minute orbit is shaded from the sun by the earth. The power budgets considered each of these two extremes.

3.4 Laser Power Requirements

3.4.1 Effect of scan pattern.

The LAWS instrument consists of a rotating telescope to distribute the shots on the ground. If the laser is fired at a constant PRF, a non-uniform distribution of shots on the ground will result. This is illustrated in Figure (3.2) which shows one quadrant of the shot pattern on the ground for five rotations of the telescope. To generate the scan pattern, a 1.5 m telescope at a nadir angle of 45 degrees rotating at 0.1 rpm was assumed. The laser pulse rate was a constant 5 Hz and the satellite ground track velocity was 7.027 $km.s^{-1}$. Each cross on the plot represents a single shot. It can be seen that the shots in the cross track direction are clustered together.

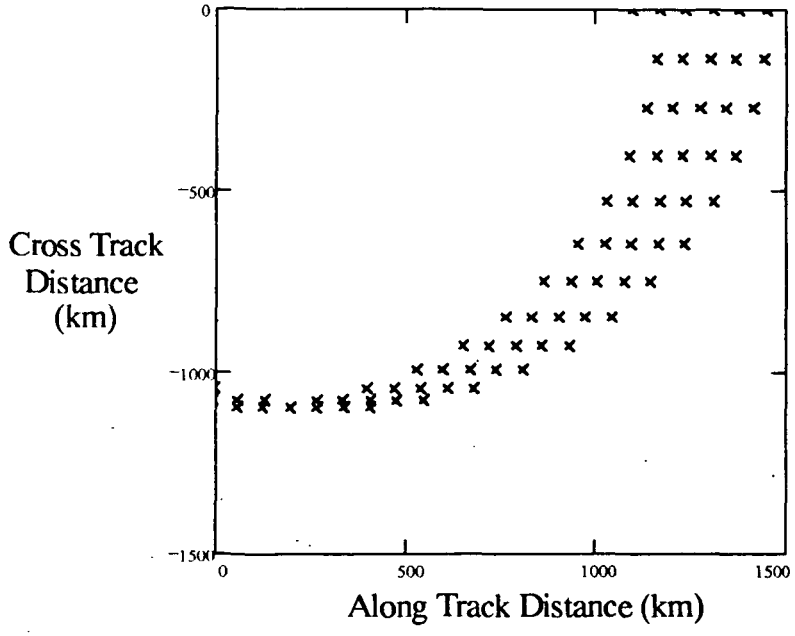

Figure (3.2) The shot pattern produced by a constant laser PRF.

To redistribute the shots more evenly, the LAWS Science Team adopted a shot pattern algorithm which varies the laser PRF with the cosine of the angle between the shot vector and the along track direction. This results in a more uniform distribution of shots which can be seen in Figure (3.3). The scan pattern shown in Figure (3.3) has the same average PRF over one scan as Figure (3.2), however the peak PRF is 7.5 Hz.

3.4.2 Latitude dependent effects.

The spacecraft orbit results in oversampling of the polar regions and undersampling of the equatorial regions. To produce more uniform coverage of the globe, the LAWS Science Team has come up with several shot patterns [3.2] which have a latitude dependent PRF component. Figure (3.4) shows the variation in average and peak PRF as a function of latitude for three schemes. The first scheme is simply a latitude independent pulse rate with the cosine scan pattern discussed previ-

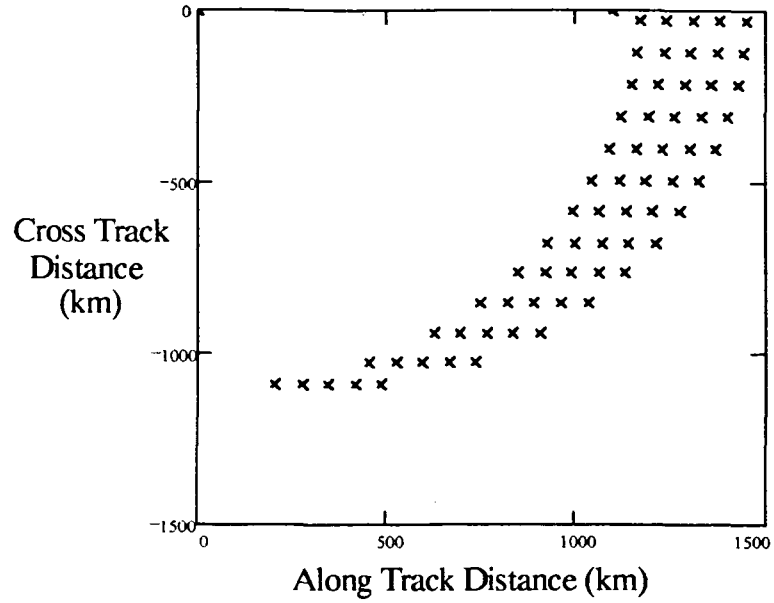

Figure (3.3) The shot pattern produced by varying the laser PRF with the cosine of the angle between the shot vector and the along track direction.

ously (Section 3.4.1). The second scheme uses an oversampling suppression algorithm to reduce the average PRF at the poles. This can be approximated by:

$$\mathrm{AVPRF}(\mathrm{latitude}) = \mathrm{PRF}_{AV}\cos(\mathrm{latitude}) \tag{3.1}$$

where PRF_{AV} is the average PRF for the latitude independent sampling scheme. The third scheme not only reduces the number of shots at the poles but also increases the number of shots at equatorial latitudes. The average PRF, over one scan, is approximated by :

$$\mathrm{AVPRF}(\mathrm{latitude}) = \mathrm{PRF}_{AV} + \cos(2 \times \mathrm{latitude}) \times (\mathrm{PRF}_{MAX} - \mathrm{PRF}_{AV}) \tag{3.2}$$

where PRF_{MAX} is the maximum PRF available from the instrument, which for the mission under consideration was 10 Hz. For both schemes, the cosine scan pattern (Section 3.4.1) is used to vary the pulse rate within a scan. This means that the peak PRF for both schemes is given by:

$$\mathrm{PKPRF}(\mathrm{latitude}) = 1.5 \times \mathrm{AVPRF}(\mathrm{latitude}) \tag{3.3}$$

The maximum pulse rate available is however limited by the laser design PRF as indicated in the previous paragraph and when this is taken into account, the PRF becomes constant within ~±30 degrees of the equator (Figure (3.4) c) for the third shot management scheme.

A Mathcad document (Appendix 3) was created to model the instrument and spacecraft power systems over one orbit. A summary of the parameters used in the model is given in Table (3.2).

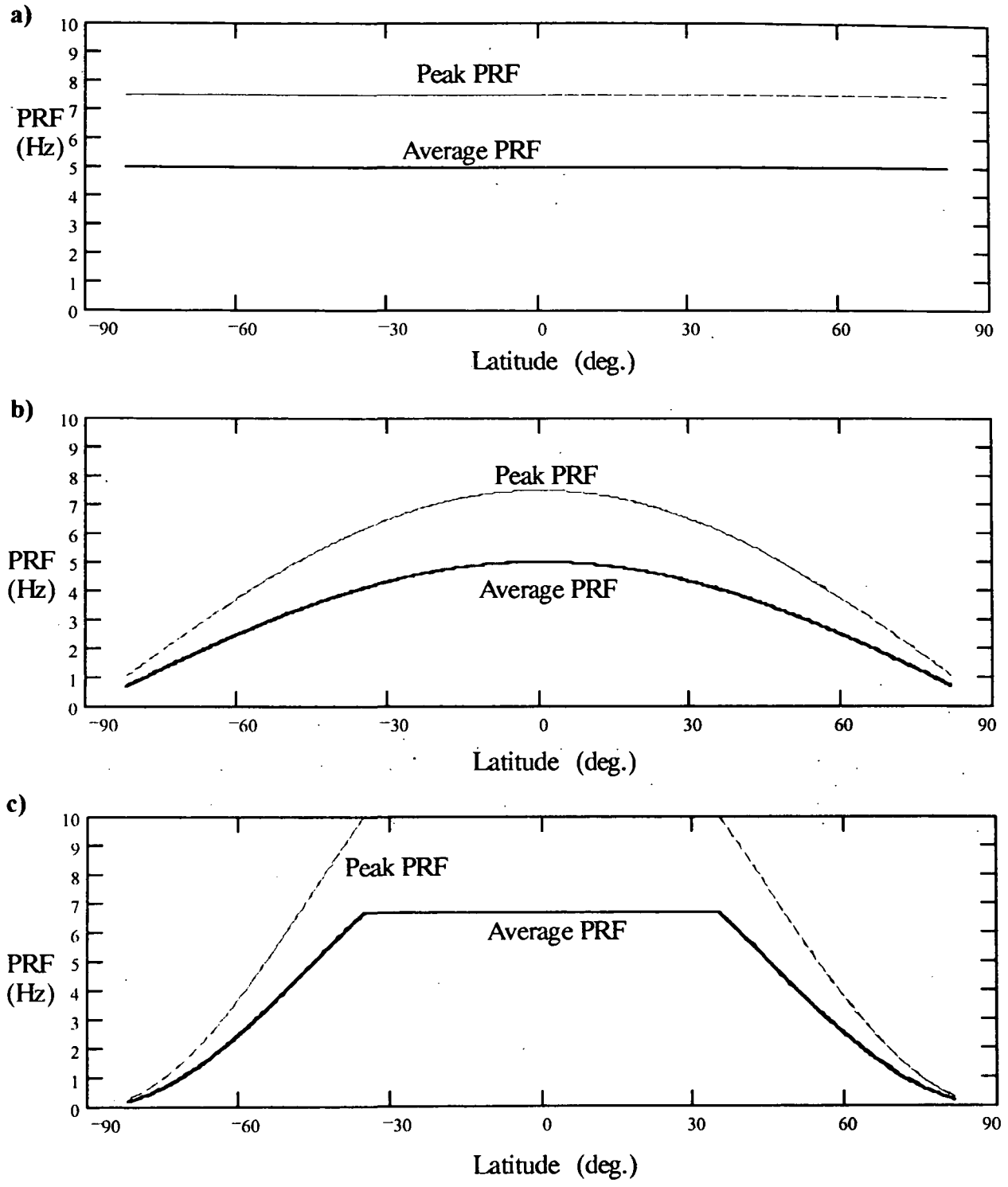

Figure (3.4) The dependence of the instrument PRF on latitude for **a)** a PRF independent of latitude, **b)** a polar oversampling suppression scheme and **c)** a polar oversampling suppression/ equatorial sampling enhancement scheme.

Satellite speed	7.6059 $km.s^{-1}$
Orbit height	525 km
Average earth radius	6371.315 km
Standby /overhead power required	540 W
Power required by satellite avionics	200 W
Solar cell losses as a fraction of the solar array power (Due to end of life degradation)	10 %
Spacecraft junction switch losses	154 W
Spacecraft distribution losses	46 W
Solar array power generation	2100 W
Laser pulse energy	5 J
Telescope scan period	10 s
Laser maximum PRF	10 Hz
Laser average PRF over one orbit (latitude independent cosine scan)	5 Hz
Worst case orbit solar occultation occurs for latitudes above	49 degrees
Number of batteries on spacecraft	4
Nominal battery voltage	28 V
Storage capacity (single battery)	40 A.hr
Discharge depth allowed on batteries (fraction of maximum capacity)	0.7
Maximum charging rate of batteries (fraction of max. cap./hr.)	0.5
Efficiency of charging battery	0.86
Efficiency of battery discharge	0.86
LAWS subsystems power conversion efficiency from spacecraft bus	0.75
LAWS laser high voltage psu efficiency (120 V to HV)	0.8
LAWS laser pulse forming network transfer efficiency to discharge	0.72
LAWS laser intrinsic efficiency	0.09

Table (3.1)Parameters for LAWS on a Spot MK2 Spacecraft.

3.5

3.6 Results

The following pages of graphs summarise the results for each of the three shot patterns. In each case three plots are shown, the variation of the laser PRF, scan average power and the fractional charge in the spacecraft batteries as a function of time.

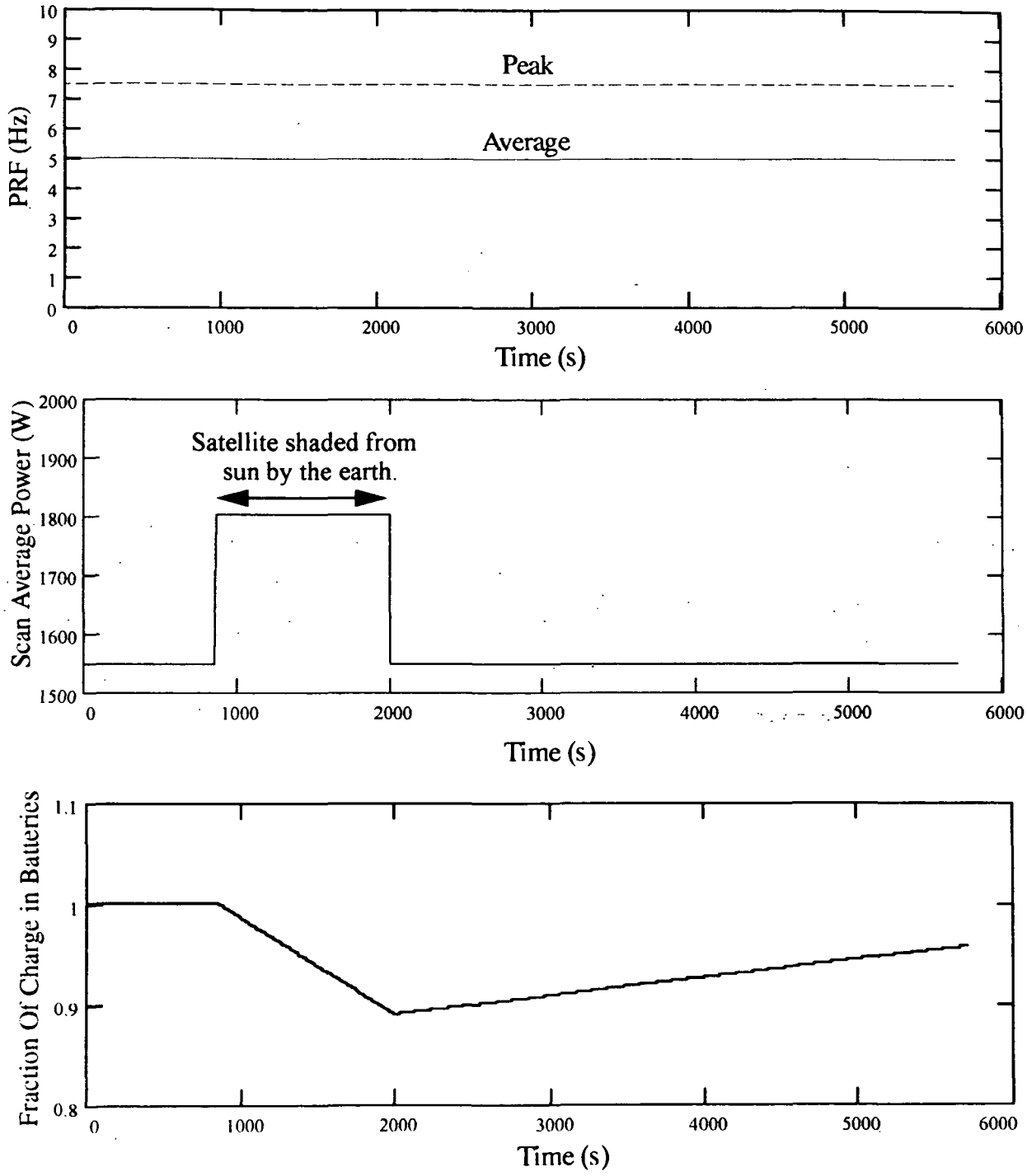

Figure (3.5) Results for the latitude independent scanning scheme.

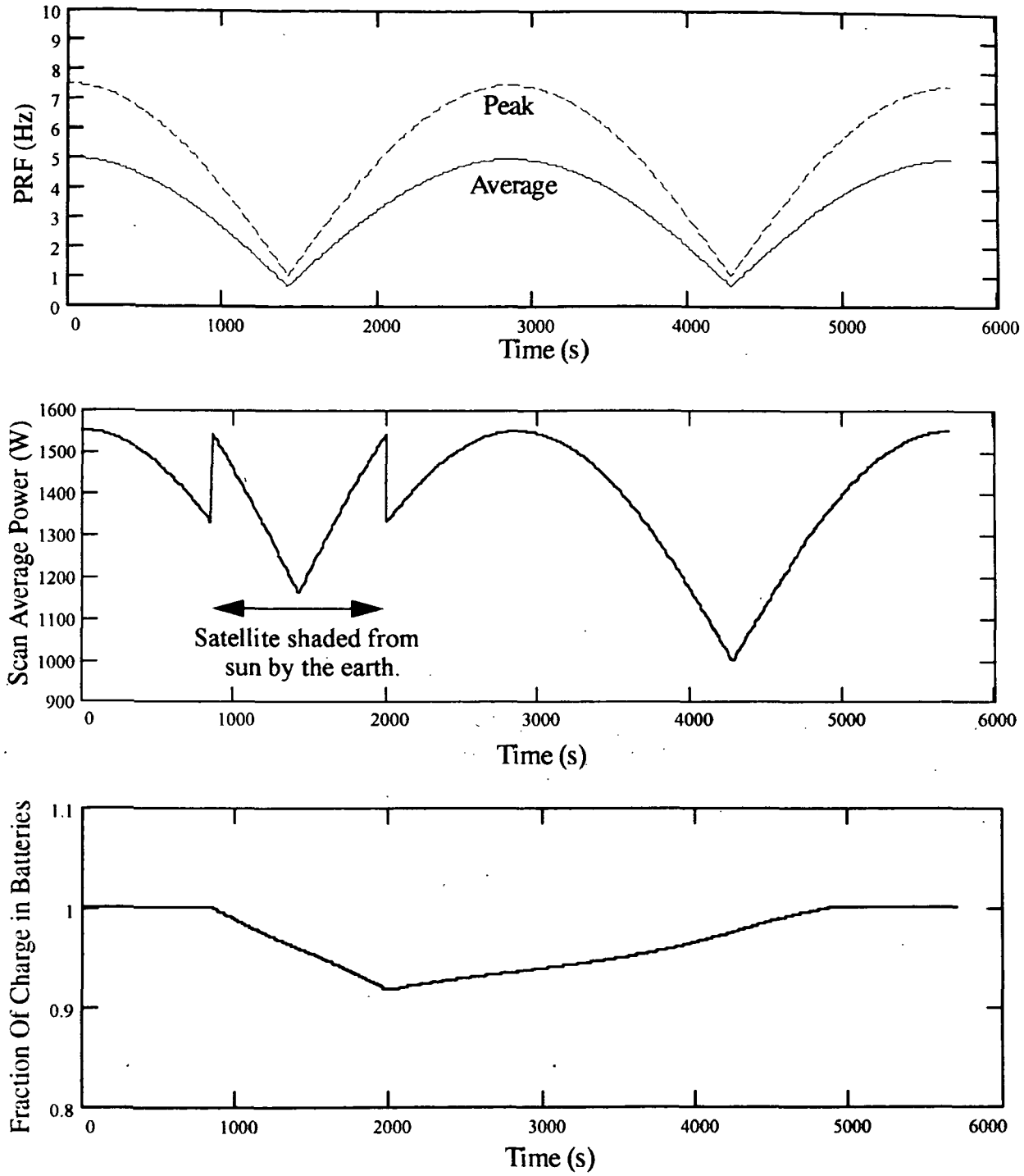

Figure (3.6) Results for the polar oversampling suppression scanning scheme.

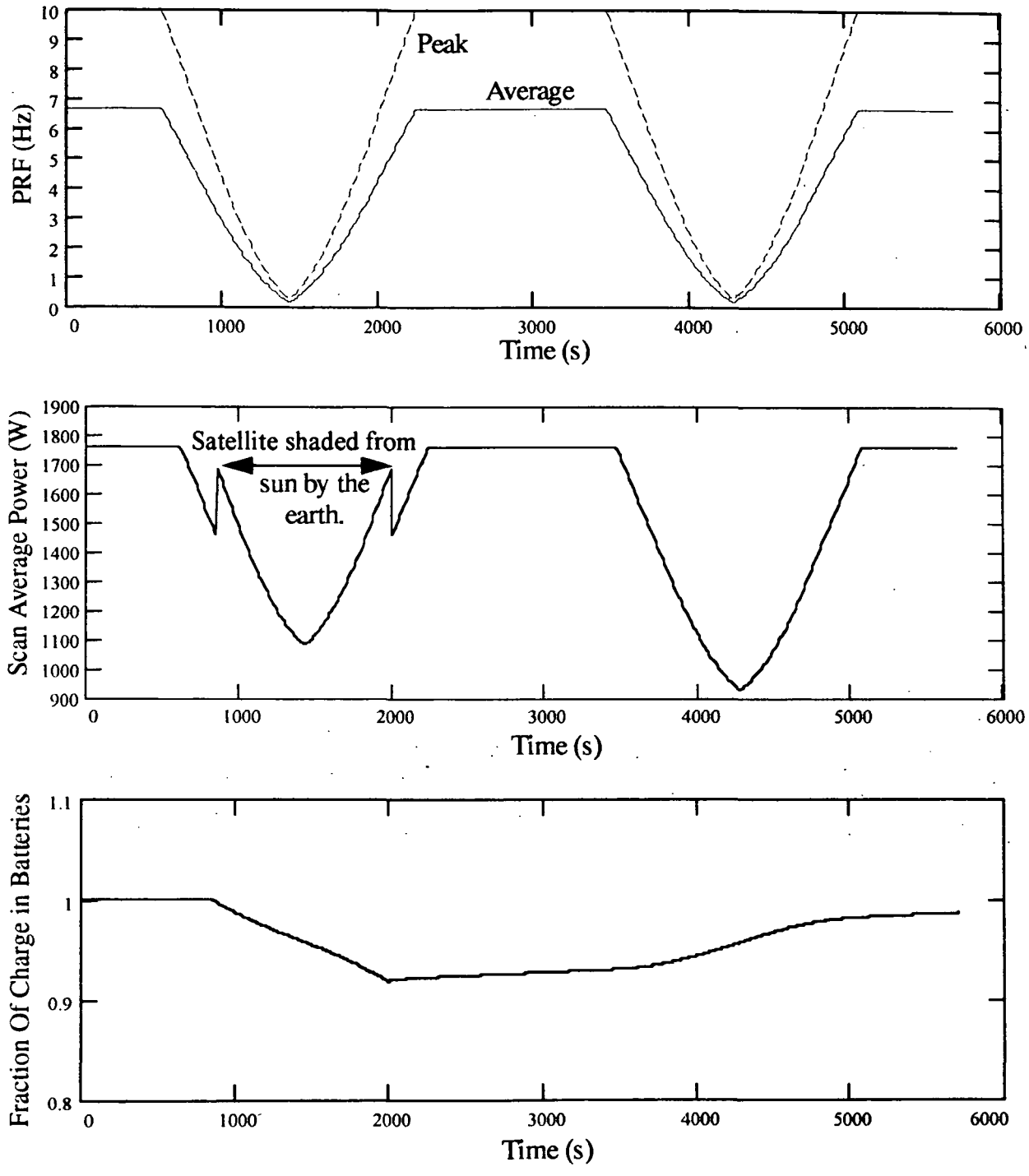

Figure (3.7) Results for the polar oversampling suppression/ equatorial sampling enhancement scanning scheme.

It can be seen from the figures that only the polar oversampling suppression scheme has enough margin to fully recharge the spacecraft batteries in one orbit. shows the power margin for each of

the schemes.

Operate Laser in Occultation	Sampling Scheme	Power Surplus (Deficit) W
Yes	Latitude independent	(89)
Yes	Polar oversampling suppression	122
Yes	Polar oversampling suppression/equatorial sampling enhancement	(19)
No	Latitude independent	61
No	Polar oversampling suppression	183
No	Polar oversampling suppression/equatorial sampling enhancement	38

Table (3.2) Power surplus (deficit) averaged over one orbit for the missions discussed in the text.

For all three scanning schemes to be useable, the solar array power must be increased by ~150 W. Alternatively, if the laser is not operated during the occultation period (plots not shown) there is sufficient power for any of the sampling schemes considered.

3.7 Conclusions

A model of the power budget for a reduced energy (5 J) LAWS system on a Spot MKII platform has been developed. The performance of the instrument/spacecraft power system was analysed for the worst case orbit and the results summarised (Table (3.2)). The model is readily changed to adapt to alternate instrument and/or satellite configurations.

3.8 References

[3.1] LAWS Phase B reports from G.E.

[3.2] Personal communication from Dr. G.D. Emmitt, Simpson Weather Associates, 809 E. Jefferson St., Charlottesville, VA 22901.

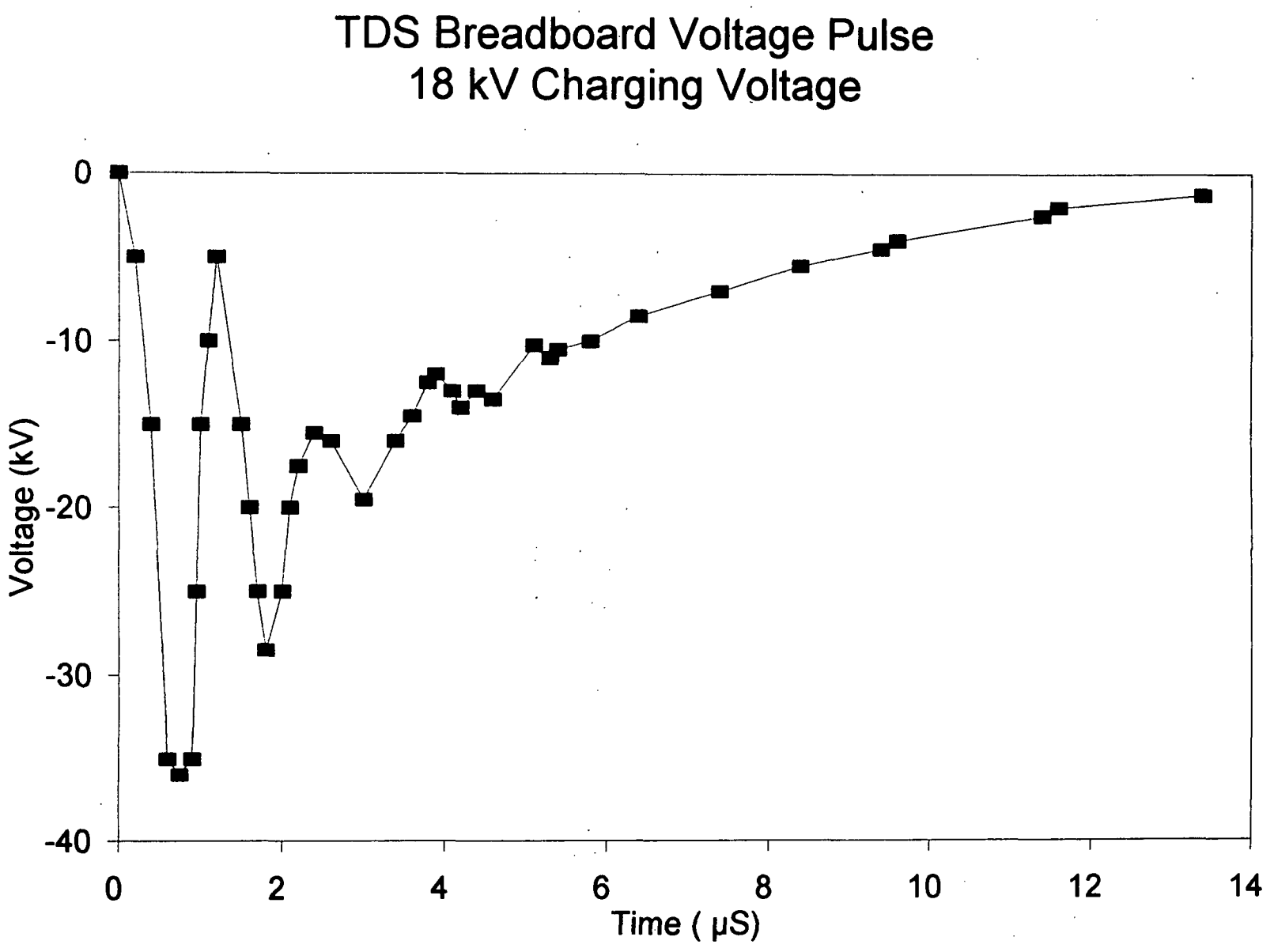

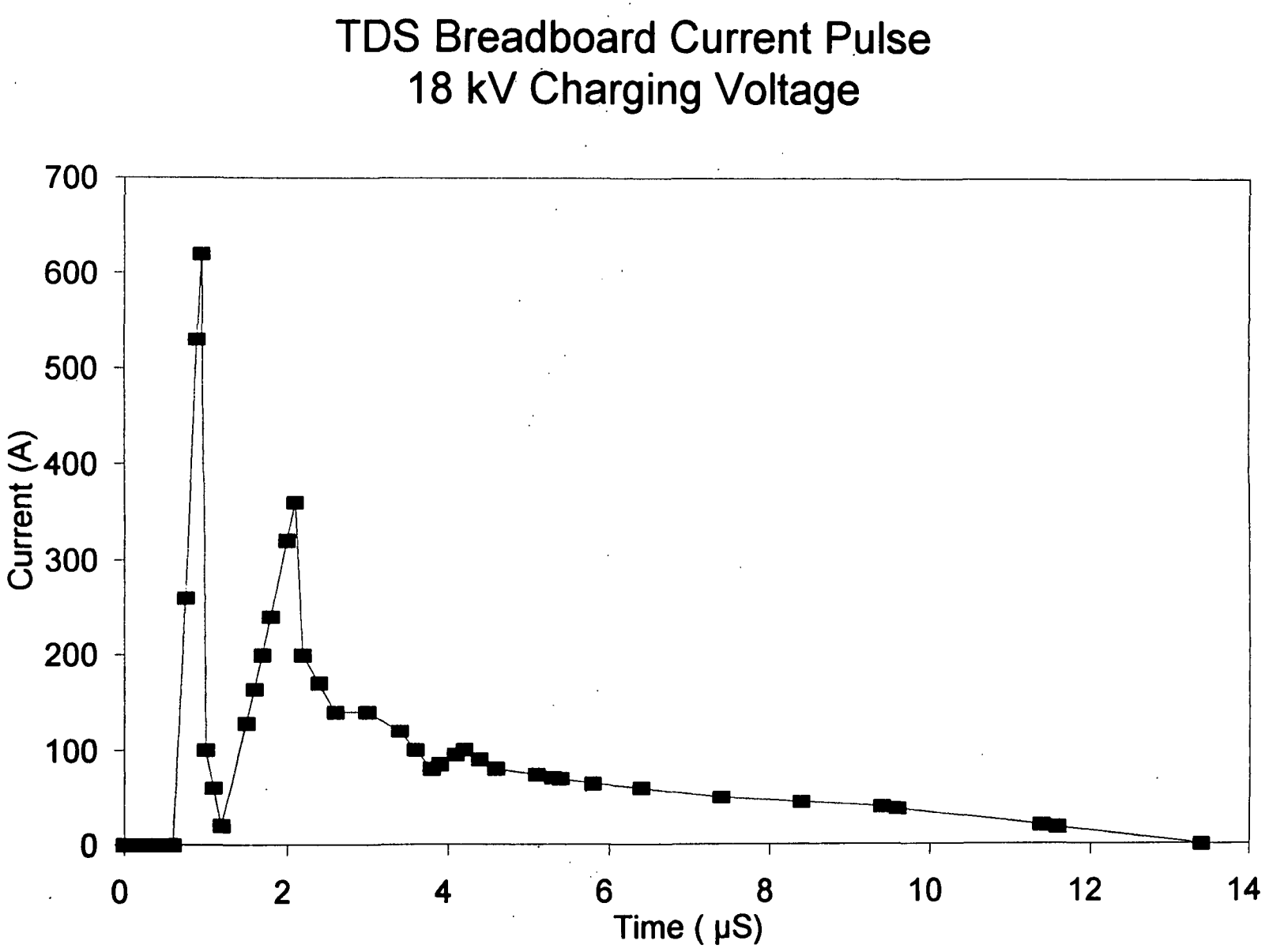

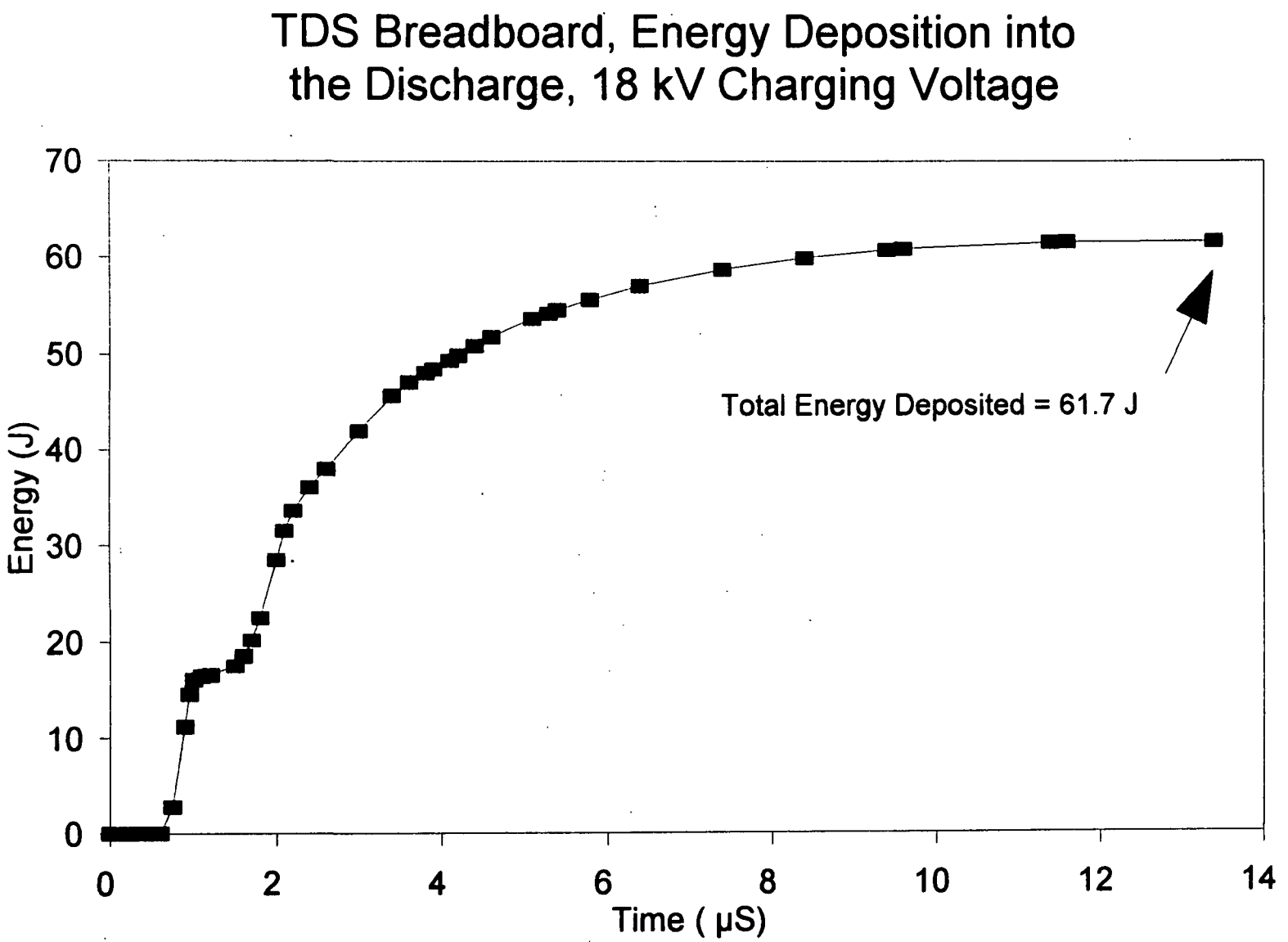
TDS Breadboard, Energy Deposition into the Discharge, 18 kV Charging Voltage
Energy (J)
70
60
50
40
30
20
10
0
0
2
4
6
8
10
12
14
Time (μS)
Total Energy Deposited = 61.7 J

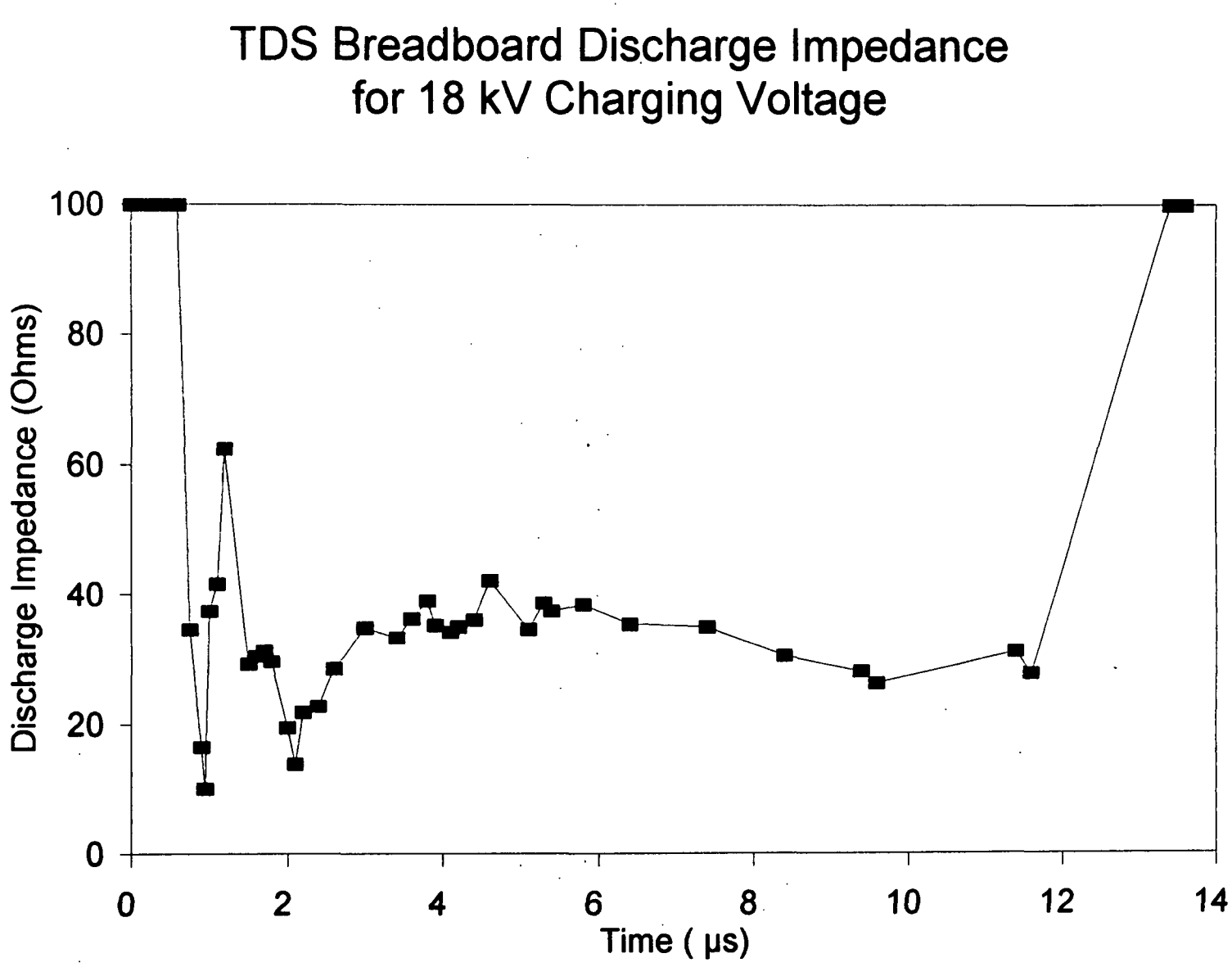

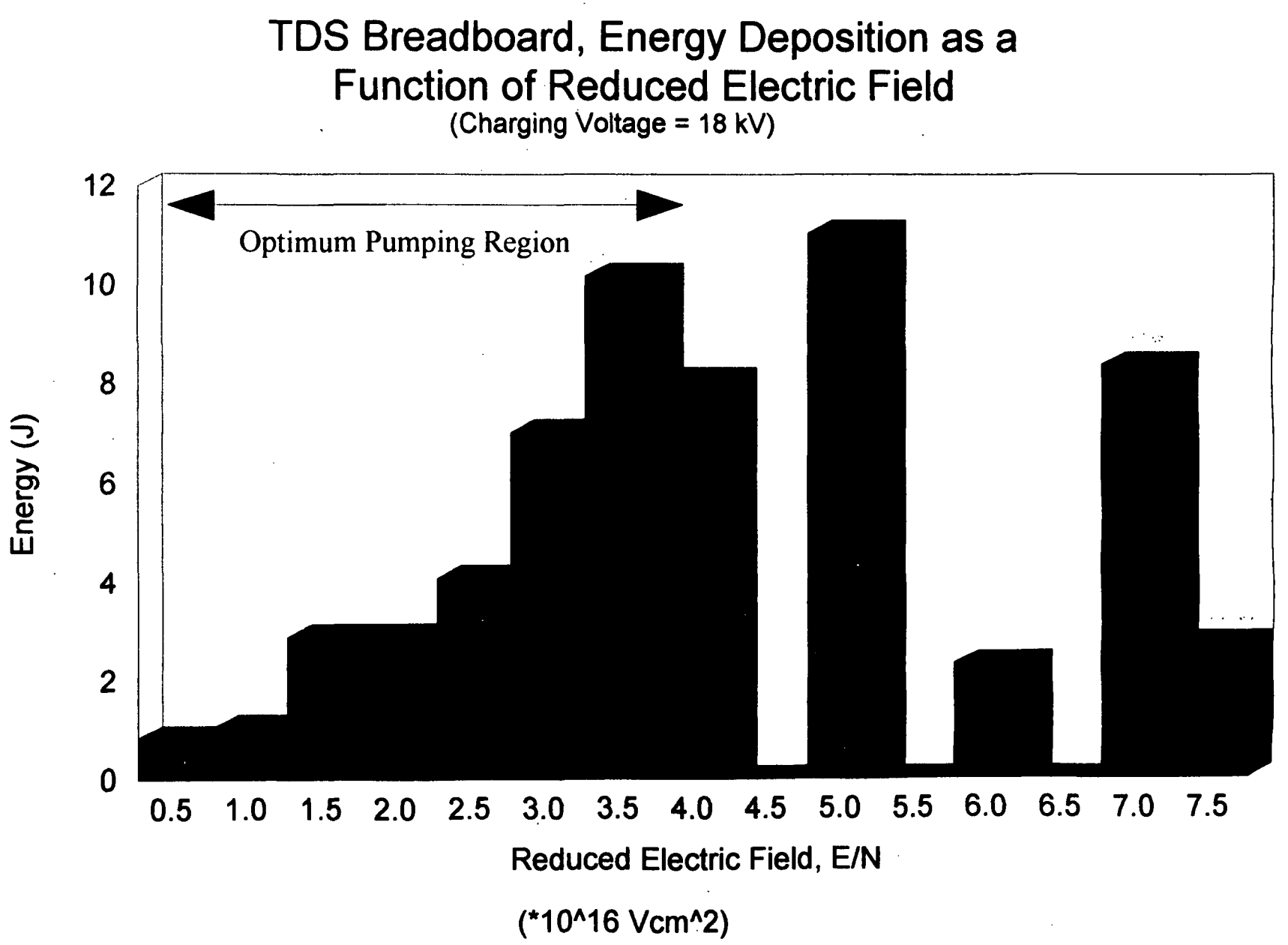

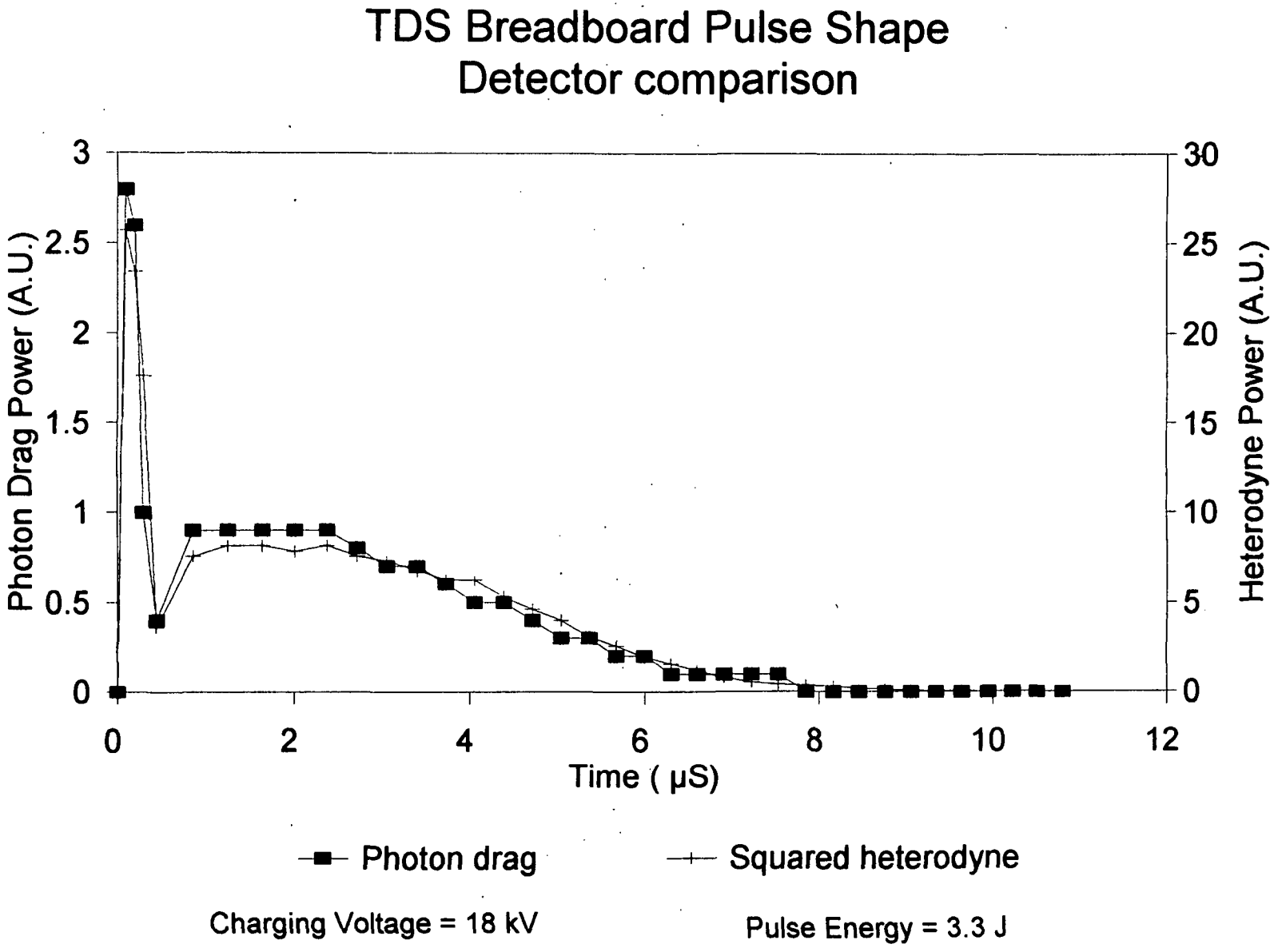

LMSC/TDS Laser Breadboard
Measured Frequency Chirp

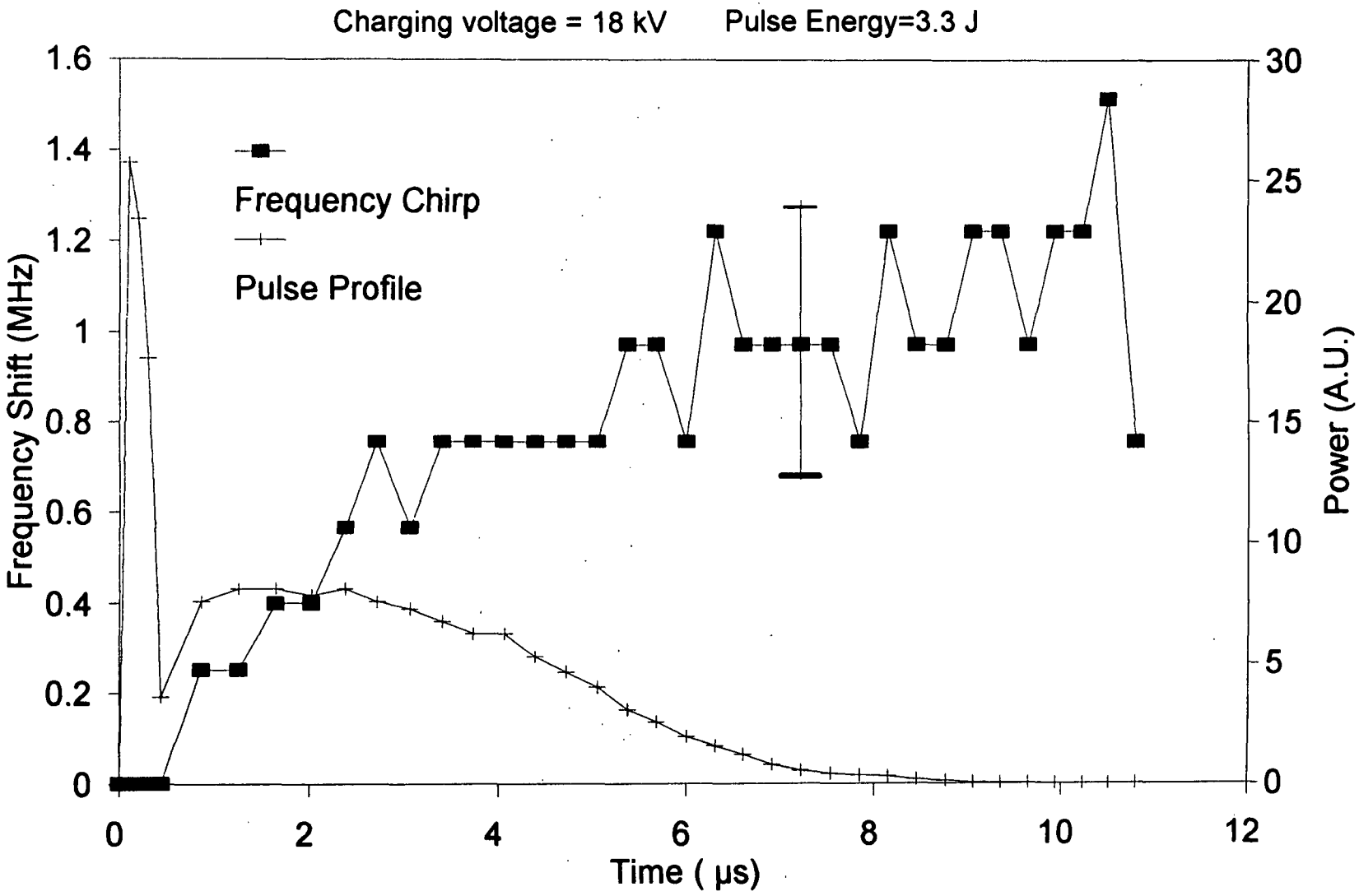

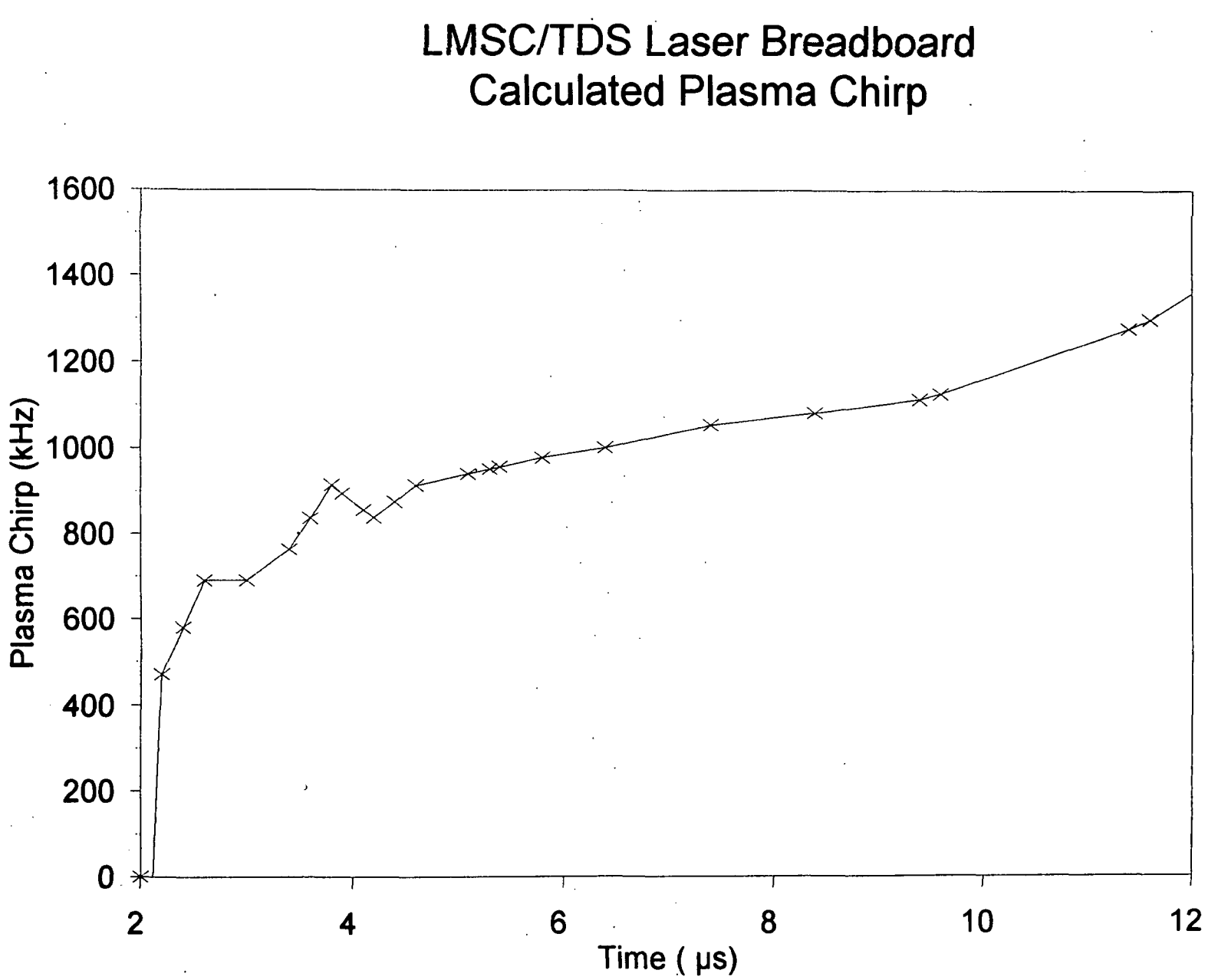

Appendix 2 - STI Optronics Breadboard Results

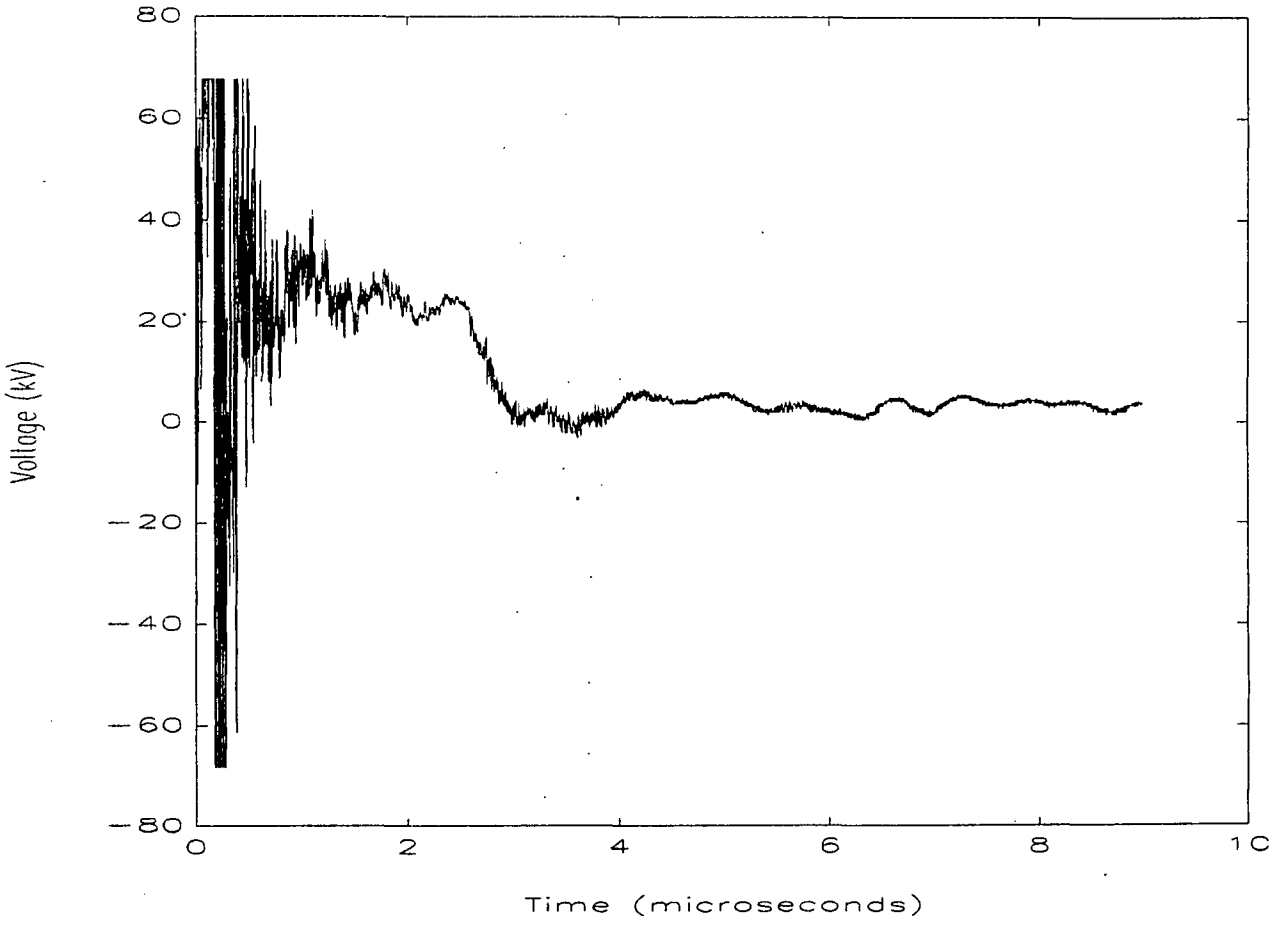

Discharge Voltage Pulse - 22.5 kV Charging Voltage

Appendix 2 - STI Optronics Breadboard Results

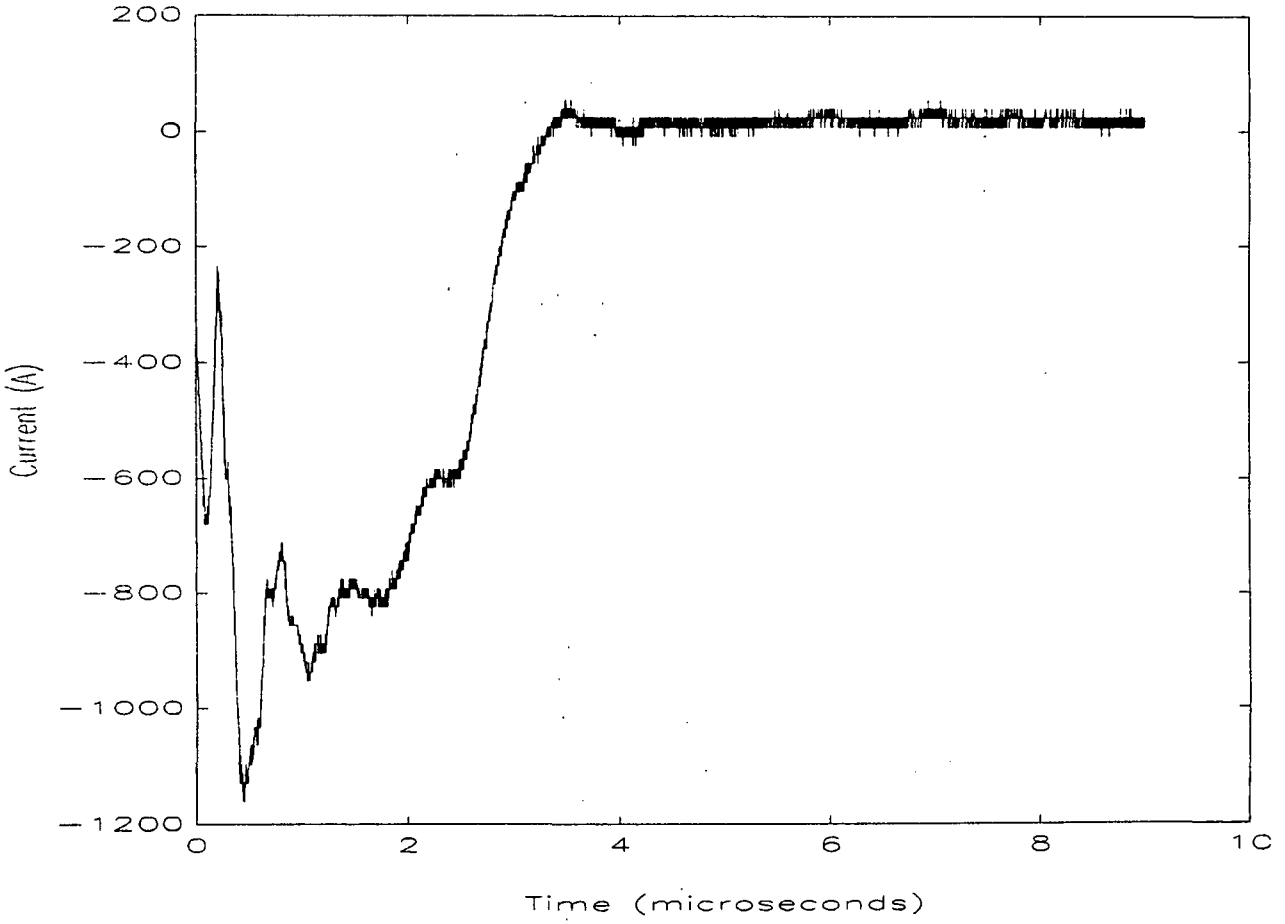

Discharge Current Pulse - 22.5 kV Charging Voltage

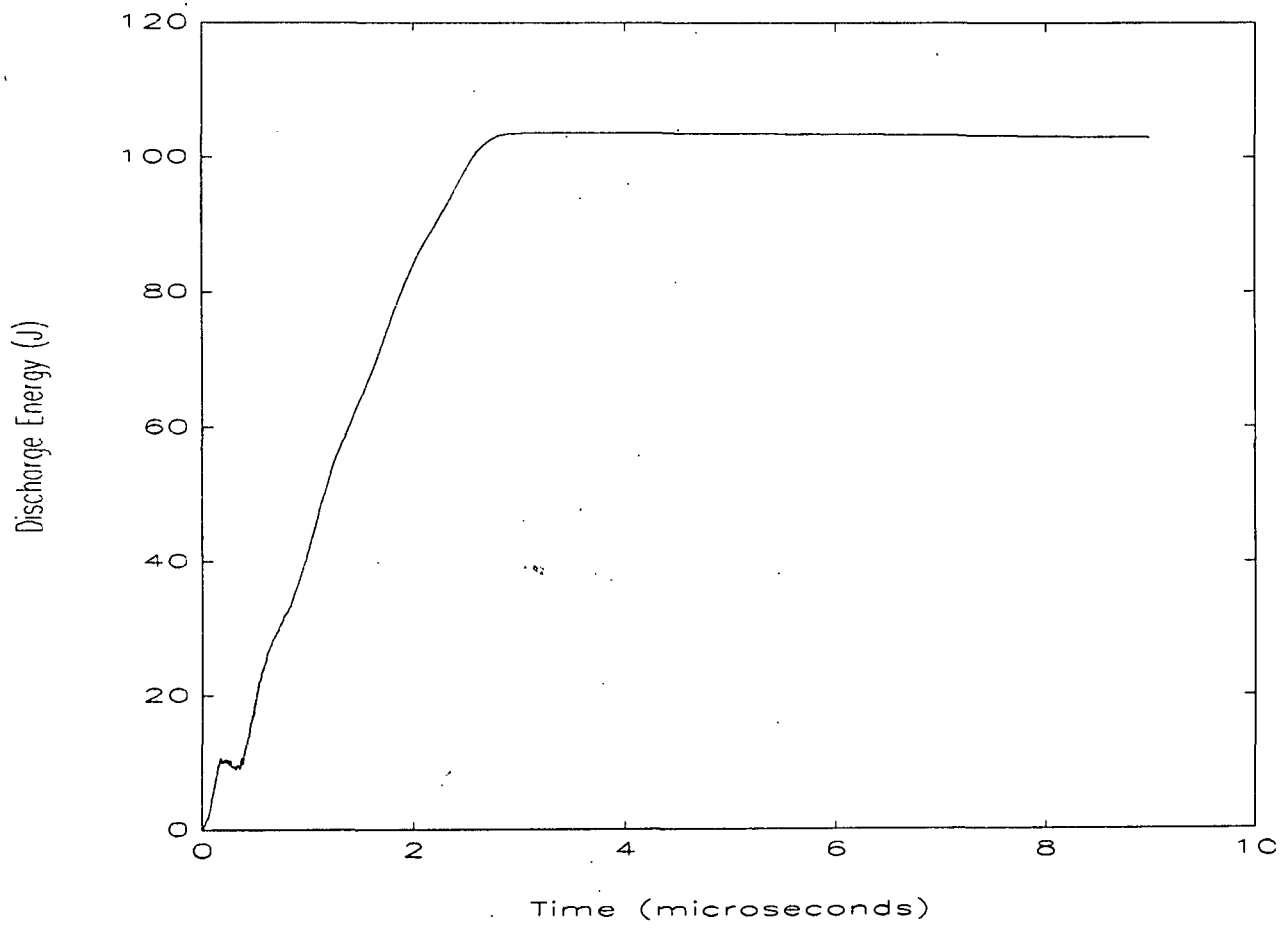

Energy Deposited into Discharge - 22.5 kV Charging Voltage

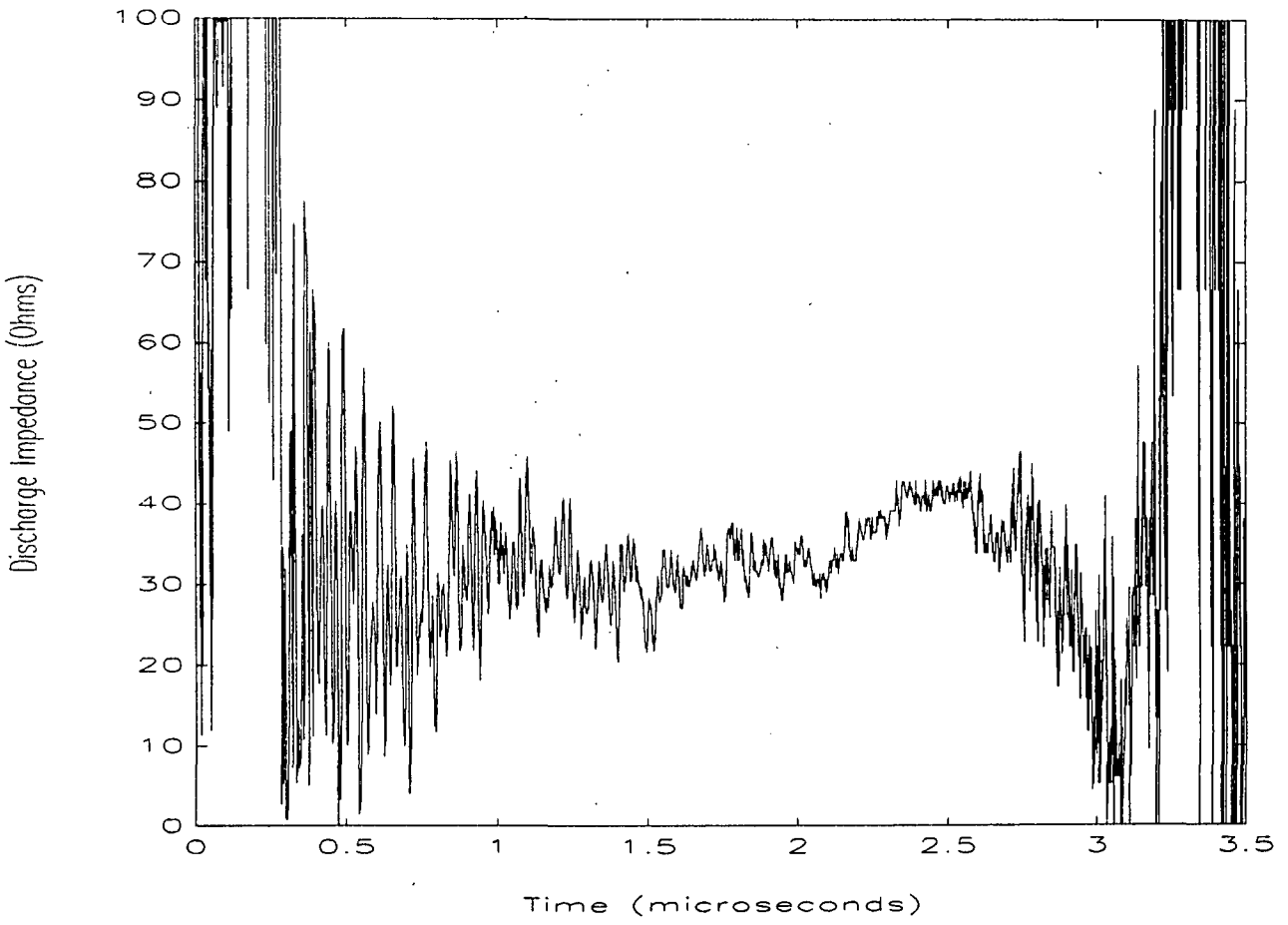

Discharge Impedance - 22.5 kV Charging Voltage

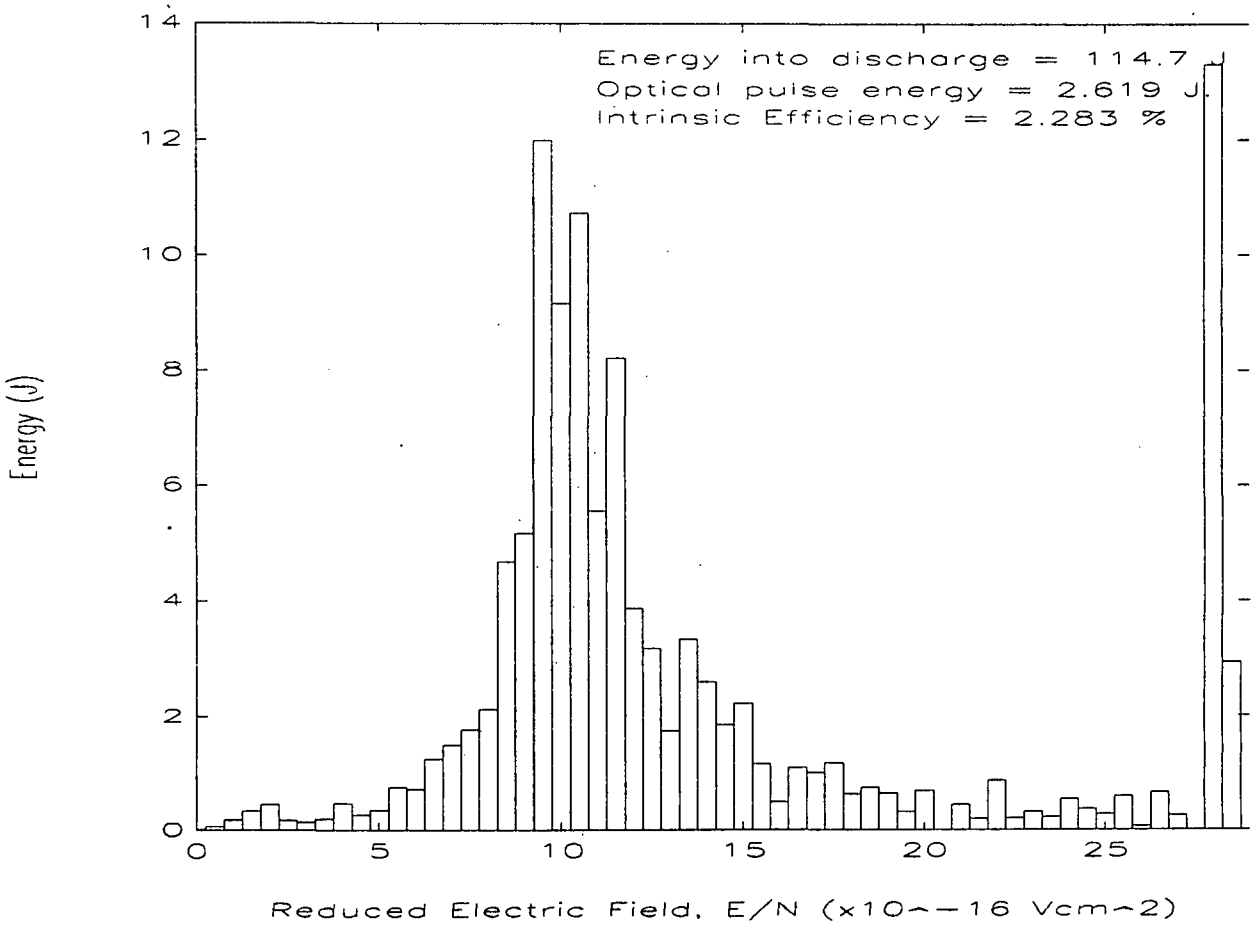

Energy Deposition as a function of Reduced Electric Field, E/N
22.5 kV Charging Voltage

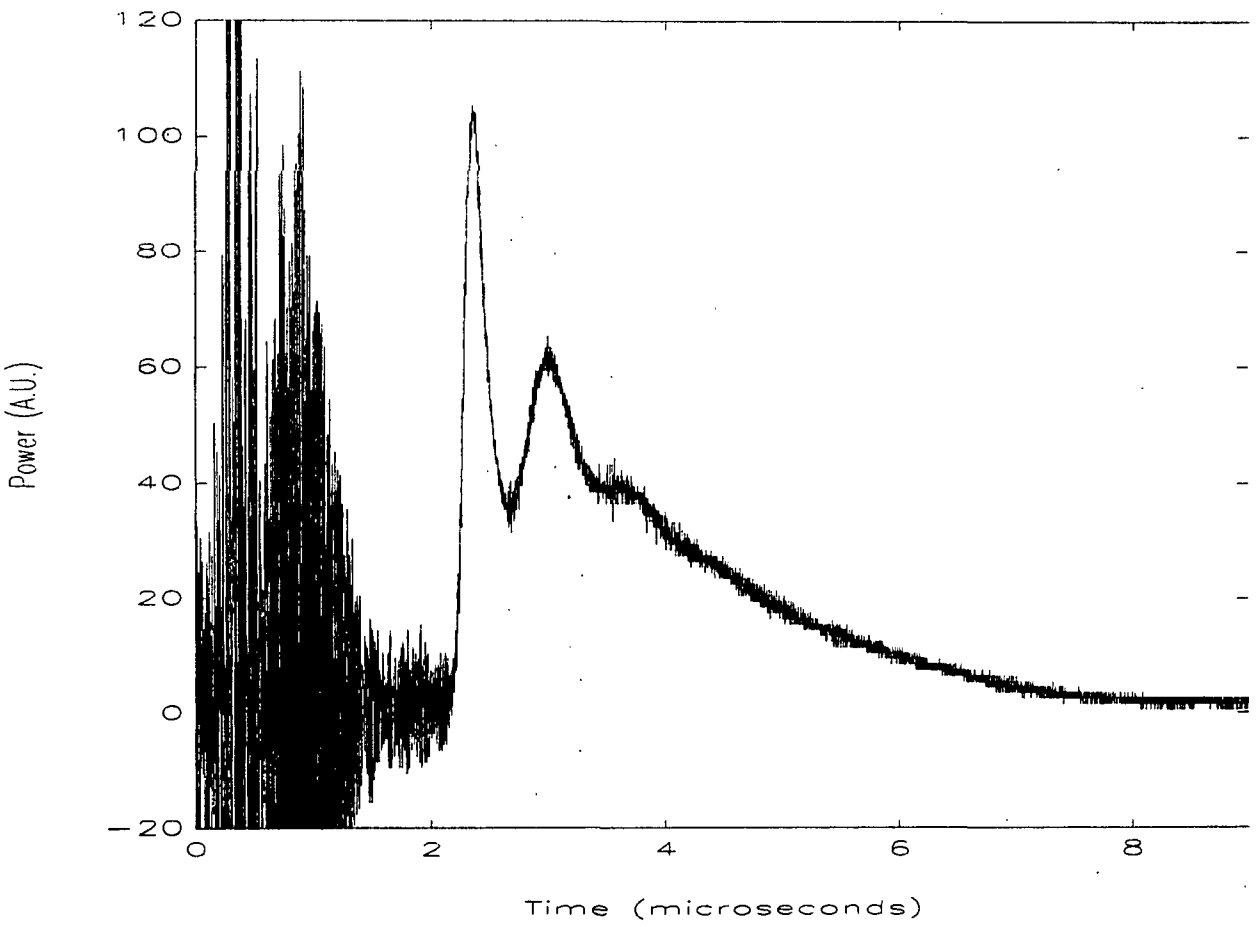

Optical Output Pulse - 22.5 kV Charging Voltage

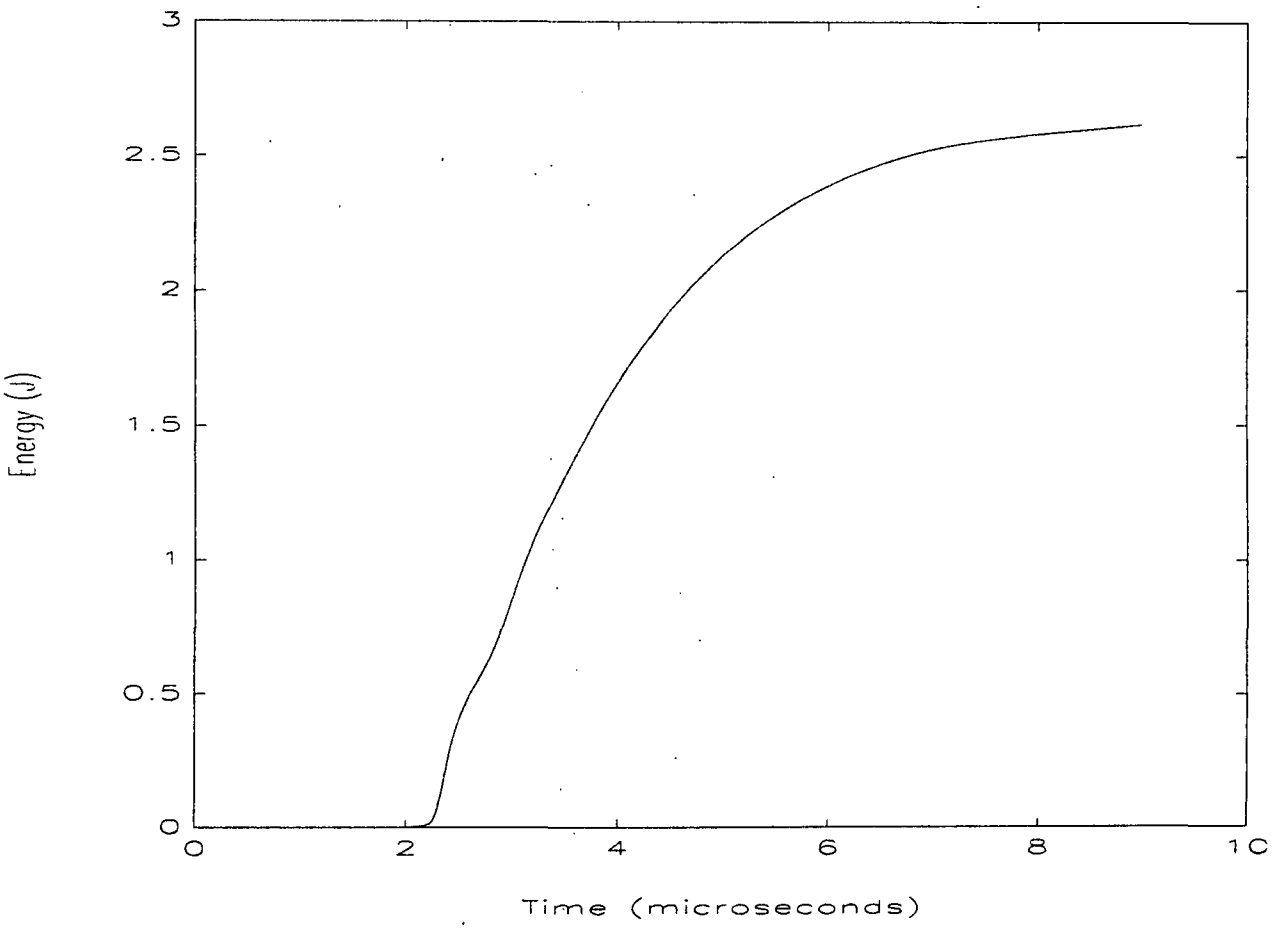

Optical Pulse Energy Evolution as a Function of Time
22.5 kV Charging Voltage

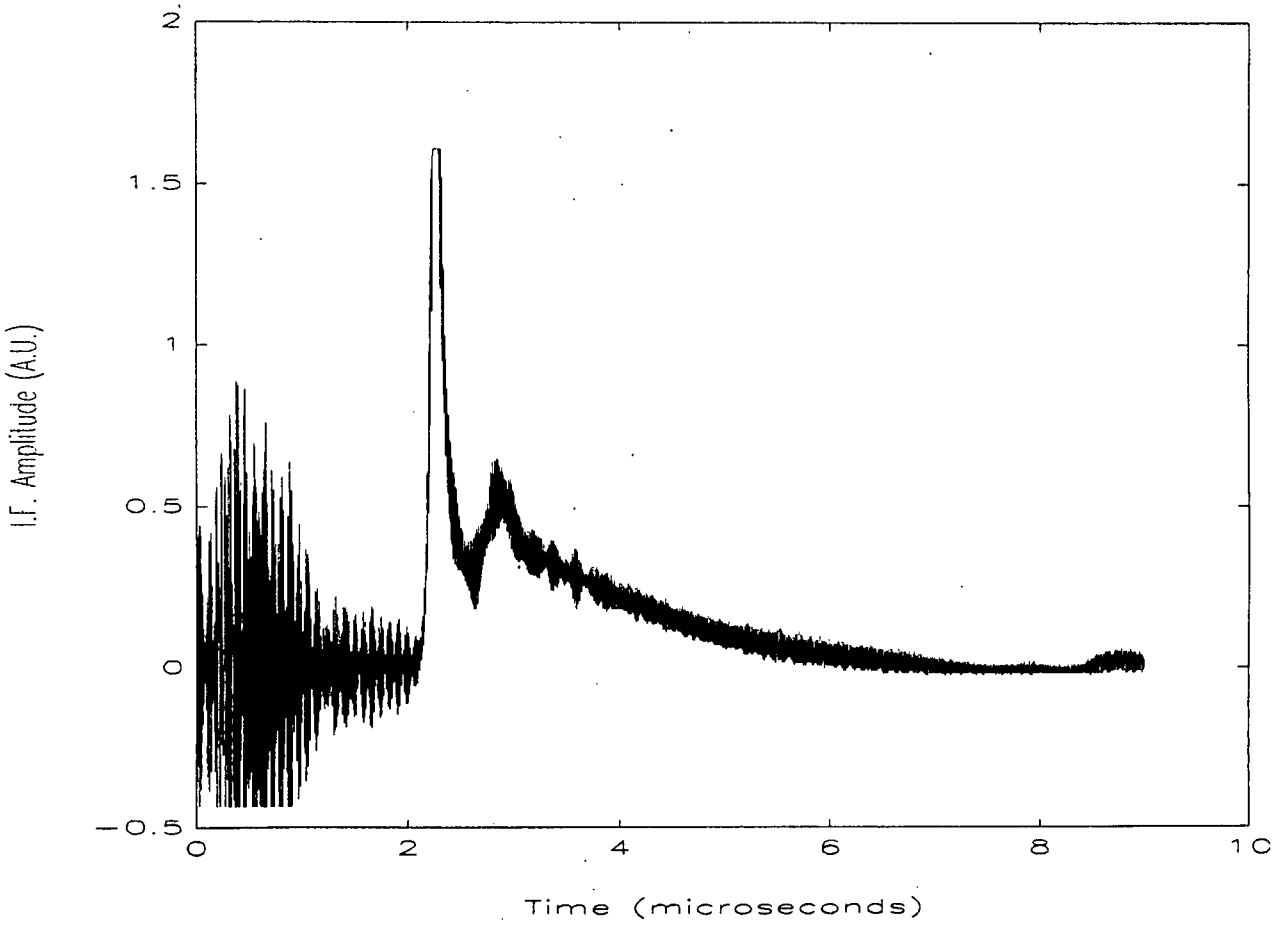

Heterodyne Beat Signal - 22.5 kV Charging Voltage

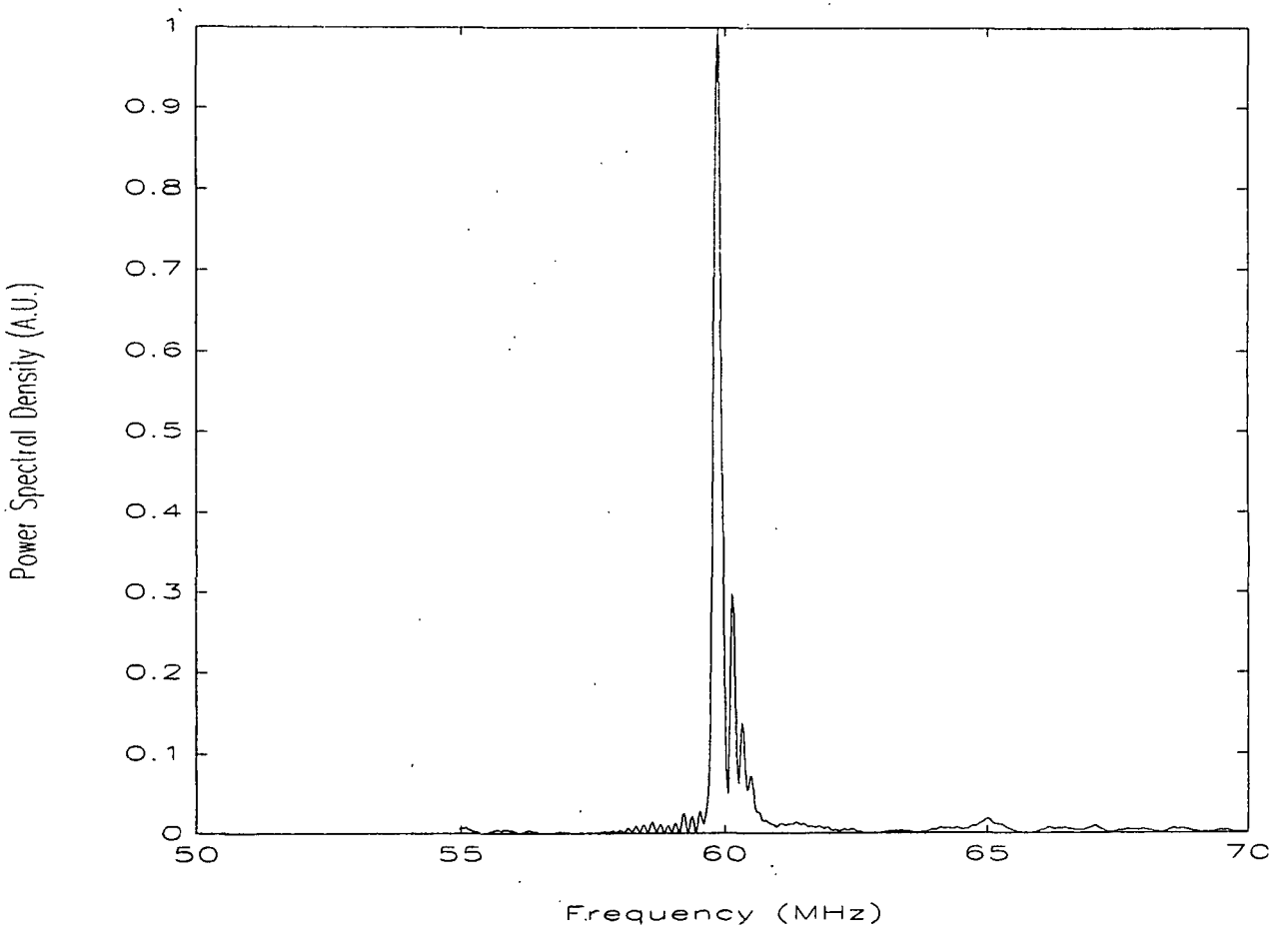

Frequency Spectrum - 22.5 kV Charging Voltage

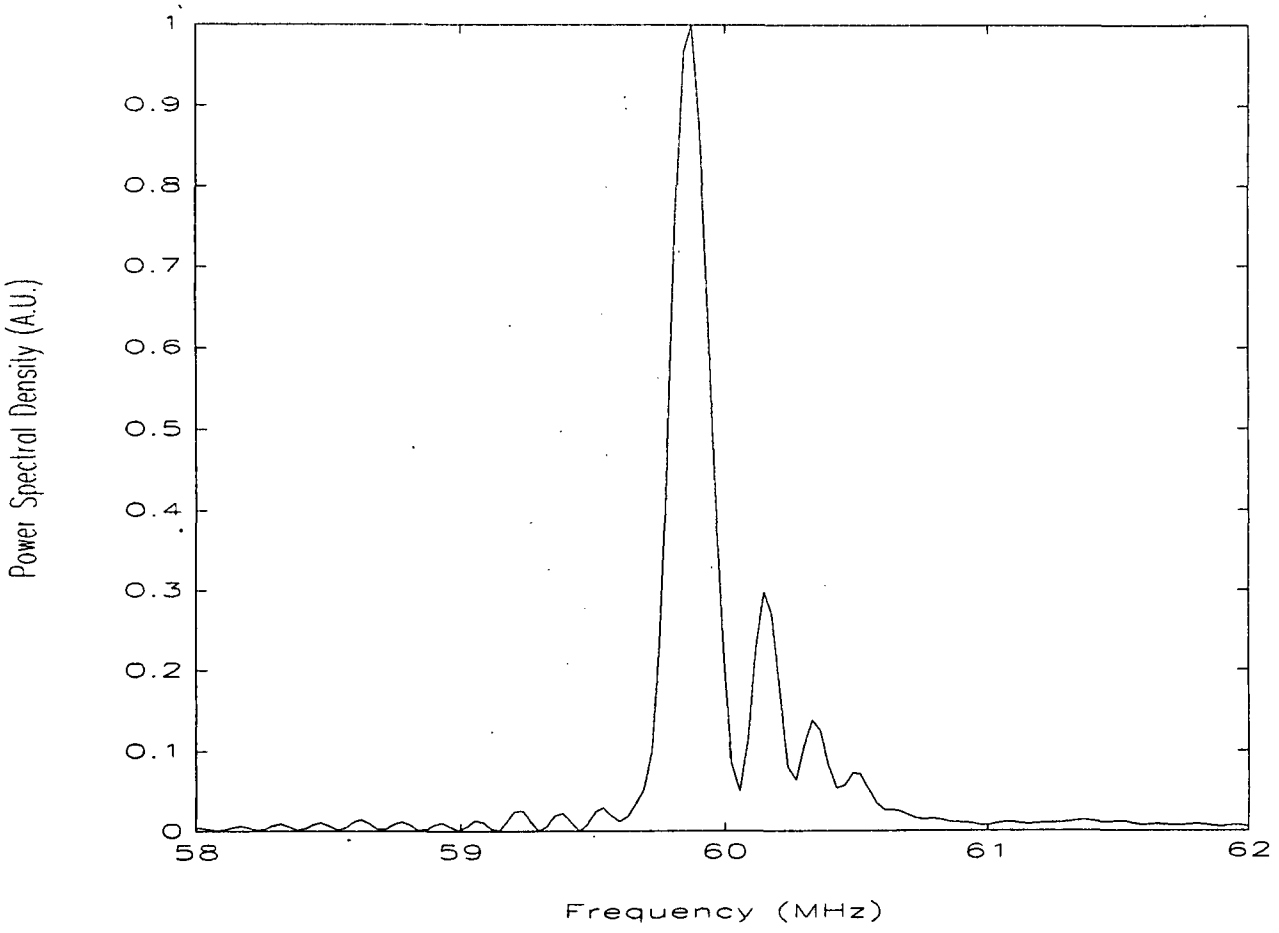

Expansion of Frequency Spectrum - 22.5 kV Charging Voltage

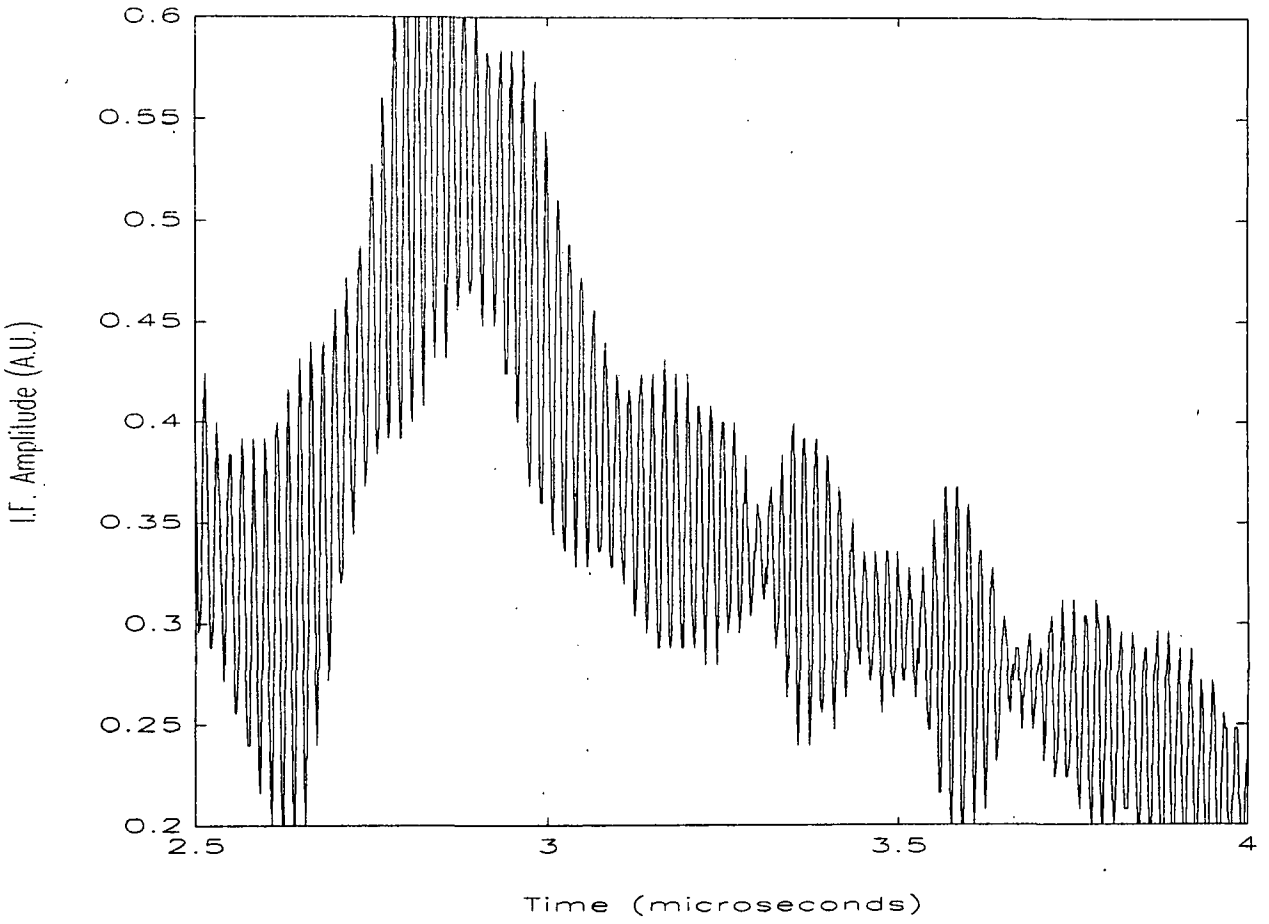

Expansion of Heterodyne Beat Frequency Signal
22.5 kV Charging Voltage

Appendix 3 LAWS Instrument Power Requirements

FILE:SPOTALL.MCD

Gary D. Spiers

This Mathcad document is based on scan algorithms provided by Dr. David Emmitt of the LAWS Science Team. The program calculates the power requirements of several scan patterns.

System Parameters

vsat := 7.6059·km·s^{-1}	Satellite speed
orbit := 525.0·km	Orbit height
earth := 6371.315·km	Average earth radius
inc := 98·deg	Orbit inclination
pstandby := 540·W	Standby/overhead power
pavionic := 200·W	Avionics power required
pulsenrg := 5·J	LAWS pulse energy
scantime := 10·s	Scan period
maxprf := 10·Hz	orbit maximum design PRF
avprf := 5·Hz	Orbit average design PRF
occult := 49·deg	Orbit occultation occurs above this latitude (set to greater than inc for all sun)
parray := 2100·W	Power generated by the solar array
amphr := 40·A·hr	Current rating of single battery
mxcharge := 0.5	Maximum charging rate as fraction of current
batdepth := 0.7	Discharge depth allowed on batteries
Vbat := 28·V	Nominal battery voltage
Nbat := 4	Number of batteries
shade := 1	Pulse laser in shade (1=Yes, 0=No)

Efficiencies

ηcharge := 0.86	Battery charging efficiency
ηdischarge := 0.86	Battery discharging efficiency
ηreg := 0.75	LAWS subsystems power conversion
ηlaser := 0.09	LAWS laser intrinsic efficiency
ηhvpsu := 0.8	LAWS laser high voltage psu efficiency (120V to HV)
ηpfn := 0.72	LAWS laser pulse forming network efficiency

Power Losses

plossarray := parray·0.1	Solar cell efficiency loss
plossjn := 154·W	Junction switch losses
plossbdu := 34·W	Spacecraft distribution losses

Derived Parameters

Orbit circumference

$$lorbit := 2\cdot\pi\cdot(orbit + earth)$$

lorbit = 43330.83·km

Orbit period

$$torbit := \frac{lorbit}{vsat}$$

torbit = 5697·s

Derived system efficiencies

$\eta pulse := \eta reg \cdot \eta hvpsu \cdot \eta pfn \cdot \eta laser$ $\eta pulse = 0.0389$

Calculate the power available whilst in the sun.

$pavbl := parray - plossarray$

Calculate orbit circumference change per degree

$$\delta lorbit := \frac{lorbit}{360 \cdot deg} \qquad \delta lorbit = 120.36 \cdot km \cdot deg^{-1}$$

Calculate latitude change

$$\delta latitude := \frac{vsat \cdot scantime}{\delta lorbit} \qquad \delta latitude = 0.6319 \cdot deg$$

Maximum energy in the batteries

$Emxbat := Nbat \cdot Vbat \cdot amphr$ $Emxbat = 4480 \cdot W \cdot hr$

Maximum rate of recharge

$Pmxchrg := mxcharge \cdot Emxbat \cdot hr^{-1}$ $Pmxchrg = 2240 \cdot W$

Calculate number of scans per orbit

$$nscan := \frac{torbit}{scantime} \qquad nscan = 569.7002$$

Set up index for calculating remaining parameters as a function of time. Take index up to first integer > nscan.

$i := 0, 1 .. ceil(nscan)$ $t_i := scantime \cdot i$

$$latitude_i := \delta latitude \cdot \frac{t_i}{scantime}$$

$latitude_i := if(latitude_i > 90 \cdot deg, 180 \cdot deg - latitude_i, latitude_i)$

$latitude_i := if[(latitude_i < -90 \cdot deg), -180 \cdot deg - latitude_i, latitude_i]$ $latitude_i := \frac{latitude_i}{90 \cdot deg} \cdot (180 \cdot deg - inc)$

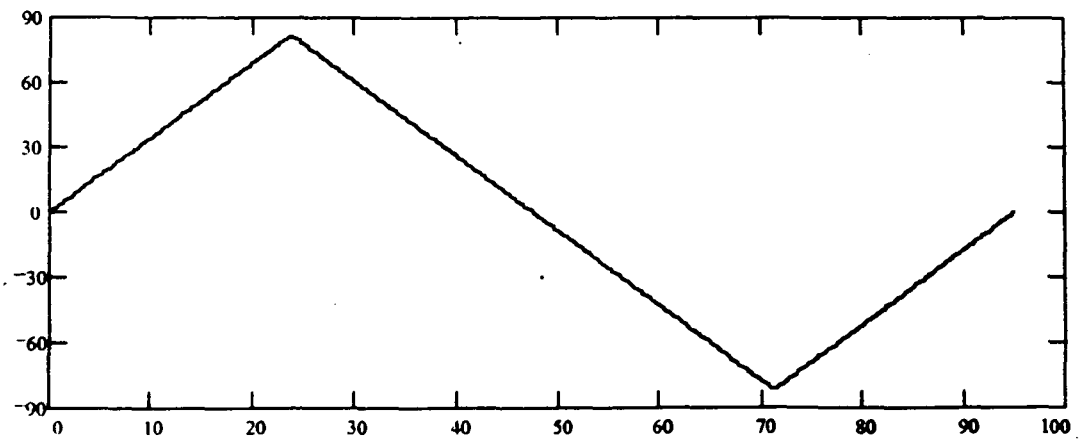

Calculate time in shade, firstly initialise to zero $tshade := 0 \cdot s$

$$tshade := \sum_i if(latitude_i > occult, scantime, 0 \cdot s) \qquad tshade = 1140 \cdot s$$

Shot management schemes

Three shot management schemes are considered, each with a flat and a peak prf requirement.

$j := 1..3$ $\quad flatprf_{i,j} := 0 \cdot Hz$ $\quad pkprf_{i,j} := 0 \cdot Hz$

1) Cosine scan.

$flatprf_{i,1} := avprf$ $\quad pkprf_{i,1} := 1.5 \cdot avprf$

2) 12 hour oversampling suppression (approximation).

$flatprf_{i,2} := \cos(latitude_i) \cdot avprf$ $\quad pkprf_{i,2} := 1.5 \cdot flatprf_{i,2}$

3) Equatorial enhancement (twice midlats), option a.

$flatprf_{i,3} := avprf + \cos(latitude_i \cdot 2) \cdot (maxprf - avprf)$ $\quad pkprf_{i,3} := 1.5 \cdot flatprf_{i,3}$

These formula may allow prfs to exceed maximum allowed value or to be less than zero, so truncate at maximum prf if necessary.

$flatprf_{i,3} := if(flatprf_{i,3} < 0 \cdot Hz, 0 \cdot Hz, if(flatprf_{i,3} > maxprf, maxprf, flatprf_{i,3}))$

$pkprf_{i,3} := if(pkprf_{i,3} < 0 \cdot Hz, 0 \cdot Hz, if(pkprf_{i,3} > maxprf, maxprf, pkprf_{i,3}))$ $\quad flatprf_{i,3} := if\left(pkprf_{i,3} = maxprf, \frac{maxprf}{1.5}, flatprf_{i,3}\right)$

Calculate power required by LAWS

First the laser pulse power required at each latitude, then add in the overhead power required. allowing for efficiencies. These calculations are done for each of the shot management schemes discussed above. In the shade more power is required due to battery inefficiency.

$lasepwr_{i,j} := flatprf_{i,j} \cdot \frac{pulsenrg}{\eta pulse}$ $\quad pstandby := \frac{pstandby}{\eta reg} + plossjn + plossbdu$

$ptotsun_{i,j} := lasepwr_{i,j} + pstandby$ $\quad ptotshade_{i,j} := if\left(shade = 0, \frac{pstandby}{\eta discharge}, \frac{lasepwr_{i,j} + pstandby}{\eta discharge}\right)$

The above assumes either sun or shade over all latitudes, the following line combines the two to produce the total power requirement as a function of latitude and sun/shade location.

$ptot_{i,j} := if(latitude_i > occult, ptotshade_{i,j}, ptotsun_{i,j})$ $\quad psun_{i,j} := if(latitude_i > occult, 0 \cdot W, pavbl)$

Now calculate the power available to charge the batteries. If in the shade the power available is zero. If in the sun the power available is the difference between the available power and the LAWS power demand multiplied by the battery charging efficiency.

$\delta p_{i,j} := psun_{i,j} - ptot_{i,j}$ $\quad pavblbat_{i,j} := if(\delta p_{i,j} < 0 \cdot W, \delta p_{i,j} \cdot \eta discharge, \delta p_{i,j} \cdot \eta charge)$

Ensure power to charge batteries is always >= 0W and that the maximum allowed charging rate is not exceeded.

$pchrg_{i,j} := if(pavblbat_{i,j} < -Pmxchrg, -Pmxchrg, if(pavblbat_{i,j} > Pmxchrg, Pmxchrg, pavblbat_{i,j}))$

Calculate charge in battery as a function of latitude assuming the battery is initially fully charged before entering the shade cycle.

$k := 1..ceil(nscan)$ $\quad batchrg_{i,j} := Emxbat$

$batchng_{k,j} := pchrg_{k,j} \cdot scantime$

$batchrg_{k,j} := if\left[(batchrg_{k-1,j} + batchng_{k,j}) > Emxbat, Emxbat, batchrg_{k-1,j} + batchng_{k,j}\right]$

Ensure that the charge stored in the batteries does not exceed the maximum storage capacity of the batteries

$$batchrg_{k,j} := if(batchrg_{k,j} > Emxbat, Emxbat, batchrg_{k,j}) \qquad espare_j := \sum_i \delta p_{i,j} \cdot scantime \qquad pspare_j := \frac{espare_j}{torbit}$$

After one complete orbit determine the charge in the batteries as a fraction of the maximum possible charge.

$$batfrac_j := \frac{batchrg_{ceil(nscan-1),j}}{Emxbat}$$

Calculate total energy put back into battery during sun cycle.

$$totbatchrg_j := \sum_i pchrg_{i,j} \cdot scantime$$

Show margins for each of the shot management schemes

1) Cosine scan margin

$pspare_1 = -89 \cdot W$ $\qquad$ $espare_1 = -5.0677 \cdot 10^5 \cdot joule$

2) 12 hr oversampling suppression margin

$pspare_2 = 122 \cdot W$ $\qquad$ $espare_2 = 6.9243 \cdot 10^5 \cdot joule$

3) Equatorial enhancement (twice midlats) margin

$pspare_3 = -19 \cdot W$ $\qquad$ $espare_3 = -1.0649 \cdot 10^5 \cdot joule$

Cosine Scan Shot Management

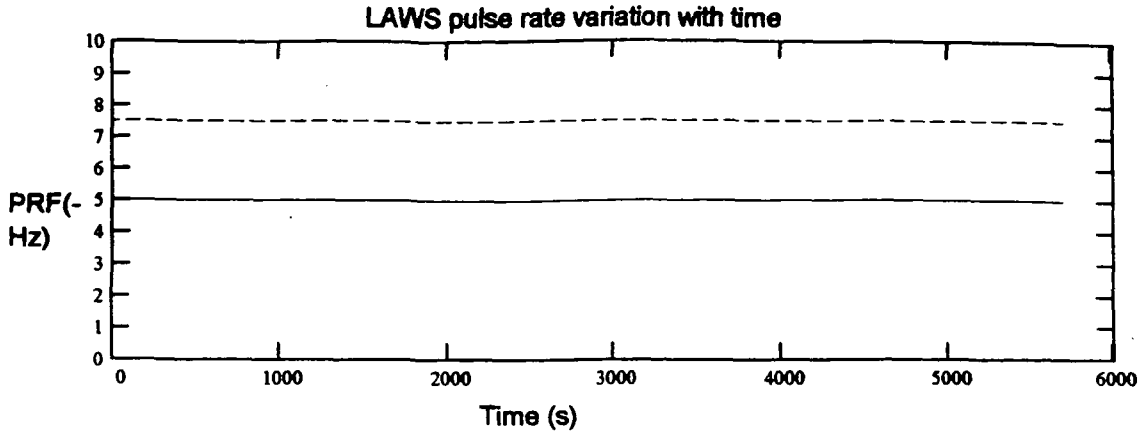

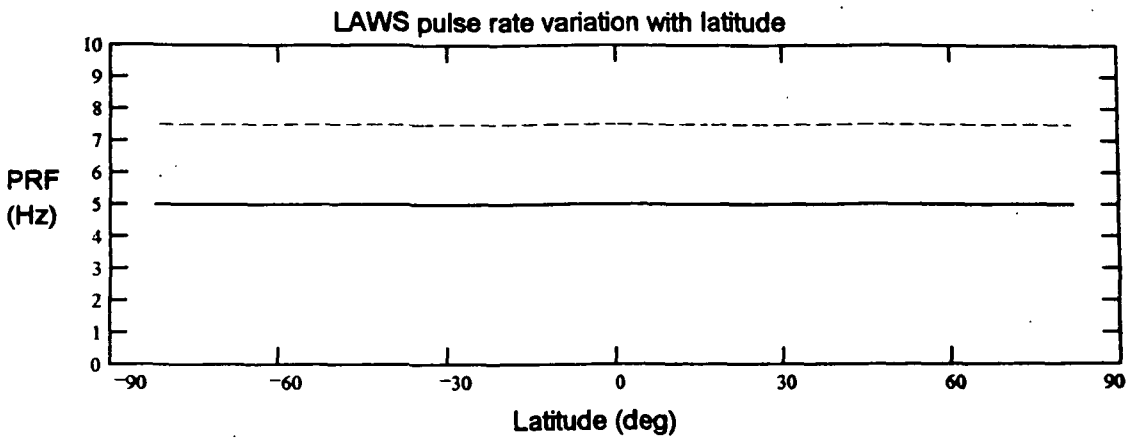

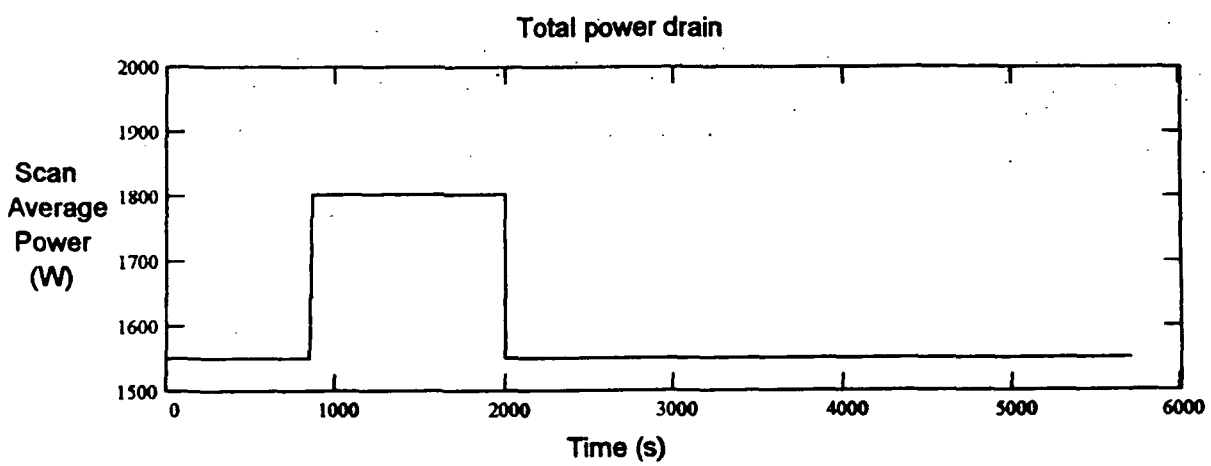

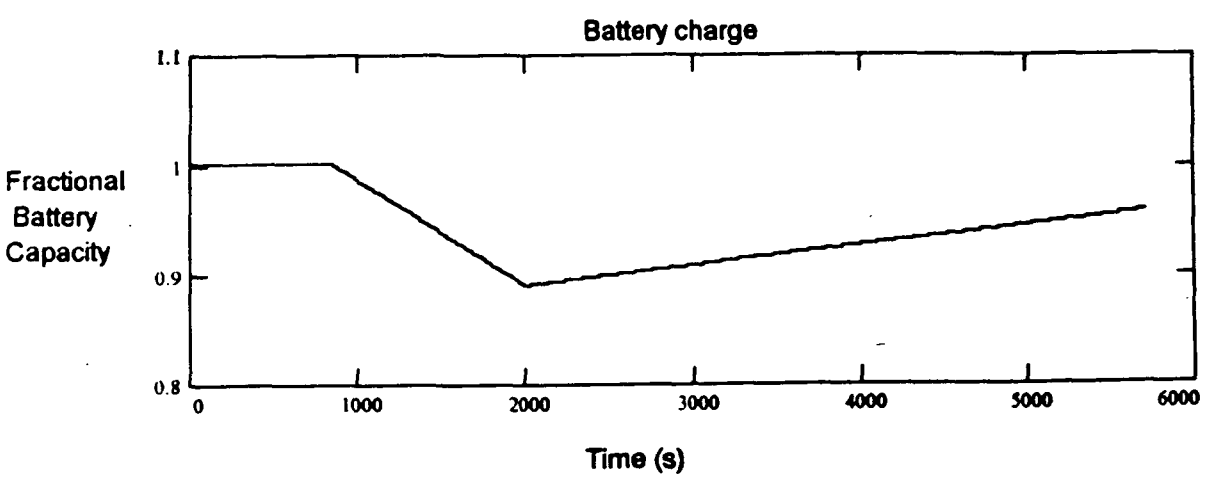

12 hour oversampling suppression

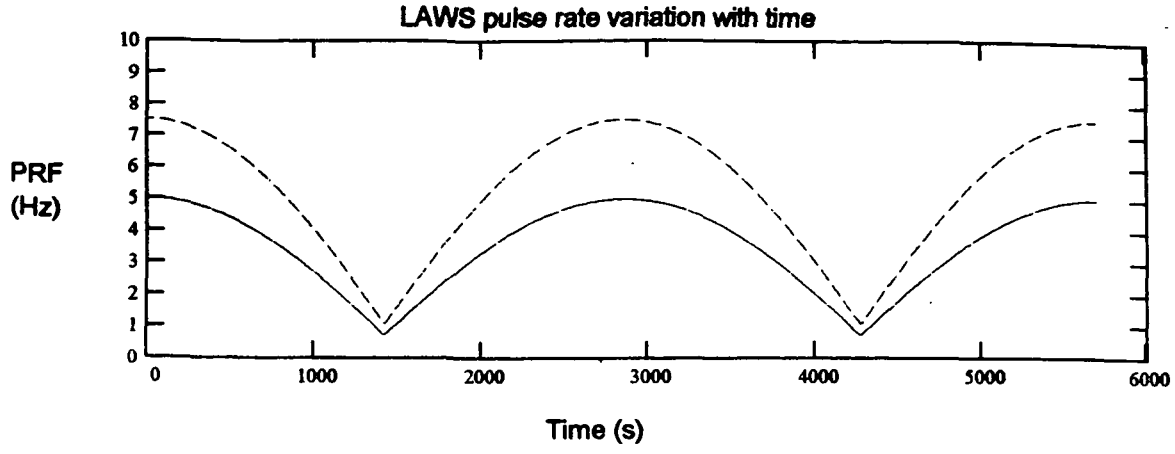

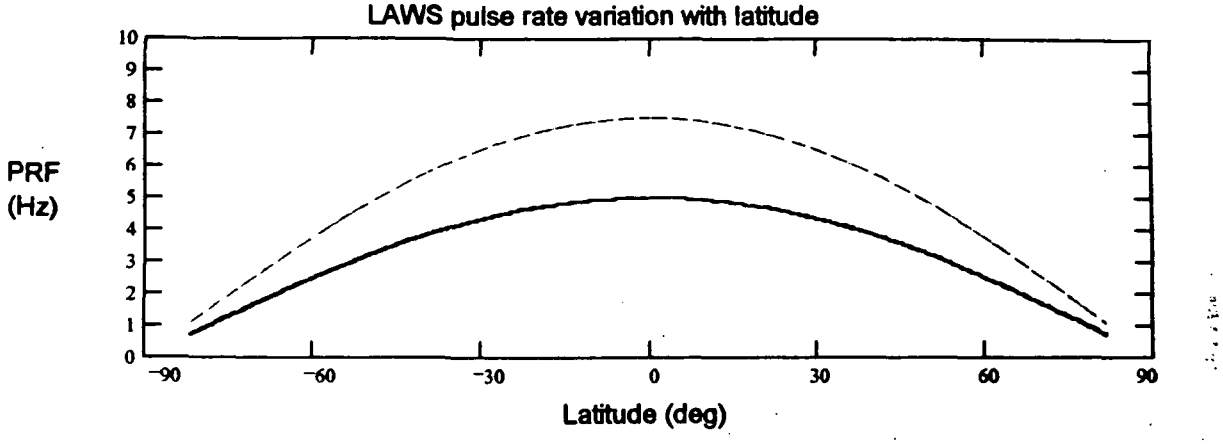

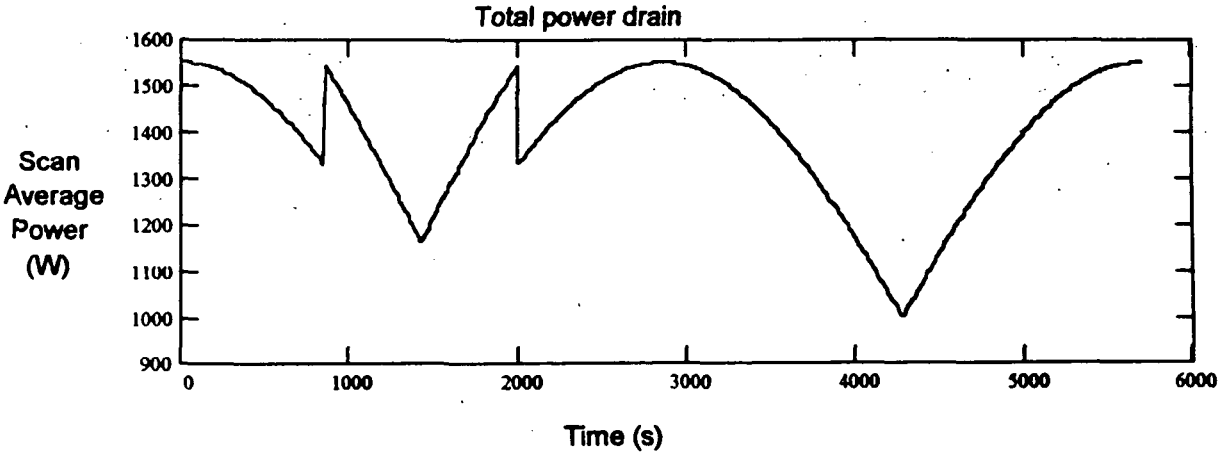

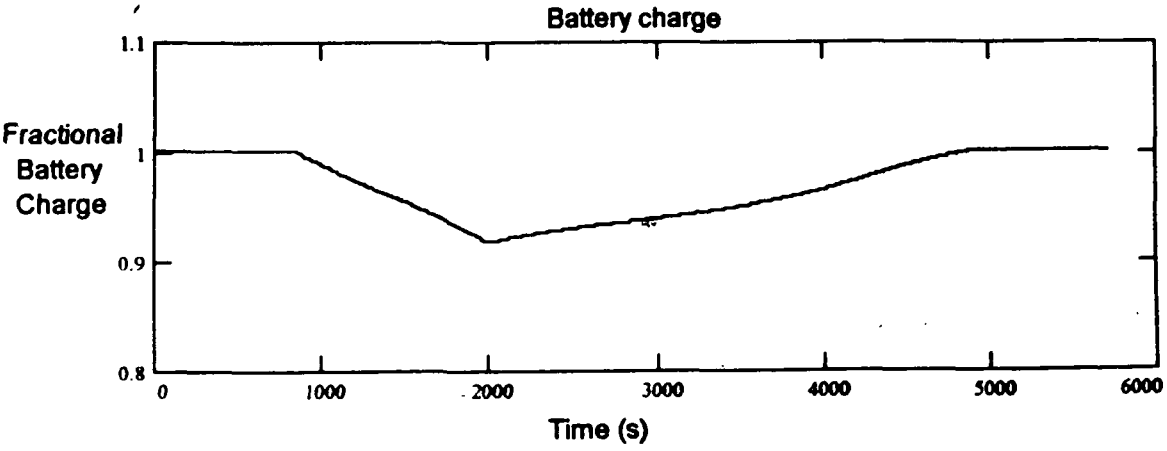

Equatorial enhancement